J. Plasma Physics (1999), *vol.* 61, *part* 4, *pp.* 553–599. Printed in the United Kingdom

Wave mixing and instabilities in cosmic-ray-modified shocks and flows

G. M. WEBB,[1] A. ZAKHARIAN[1] and G. P. ZANK[2]

[1]Lunar and Planetary Laboratory, University of Arizona, Tucson, AZ 85721, USA

[2]Bartol Research Institute, University of Delaware, Newark, DE 19716, USA

(Received 10 March 1998 and in revised form 3 August 1998)

Wave mixing equations describing the interaction of short-wavelength sound waves and entropy waves in two-fluid cosmic ray hydrodynamics in a non-uniform, large-scale, background flow in one Cartesian space dimension are investigated. The wave interaction coefficients depend on large-scale gradients in the background flow, and consist of two physically distinct components. The first component consists of wave-damping terms due to the diffusing cosmic rays, plus squeezing instability terms associated with the large-scale cosmic ray pressure gradient. These effects were first investigated by Drury and Dorfi in a study of the propagation of short-wavelength WKB sound waves in cosmic-ray-modified flows and shocks. The second component describes gas dynamical wave mixing effects due to gradients of the gas entropy S and the gas dynamical Riemann invariants ($R^{\pm}$) of the background flow. A Green function solution is used to illustrate the coupling of the backward and forward sound waves for the case of a uniform background flow, in which the coupling coefficients depend on the parameter $\alpha = a_c^2/2\kappa$, where a_c is the cosmic-ray 'sound speed' and κ is the hydrodynamical cosmic-ray diffusion coefficient. Analytical WKB approximation methods and numerical simulations are used to investigate the modifications of the cosmic ray squeezing instability by wave mixing in cosmic-ray-modified shocks and pressure balance structures. Astrophysical applications to instabilities in supernova remnant shocks are discussed.

1. Introduction

The initial work on diffusive acceleration of energetic charged particles at plane shocks, without losses (Krymsky 1977; Axford et al. 1977; Bell 1978; Blandford and Ostriker 1978) showed that energetic test particles (cosmic rays) were accelerated into a power-law momentum spectrum from scattering backward and forward across the shock. For strong shocks, with compression ratio of four, the steady-state particle pressure in the test particle solutions diverged, indicating the need for a nonlinear analysis taking account of the reaction of the energetic particles back on the flow. In applications of the theory to real astrophysical shocks, due account needs to be taken of the finite time scale for diffusive shock acceleration and particle energy losses (see e.g. Drury 1983). The energy density of the accelerated particles in strong shocks may increase to such an extent that the energetic particle pressure gradient acts back on the upstream flow, thus leading to modification of the shock by the cosmic rays.

Two-fluid hydrodynamical models of diffusive shock acceleration were developed by Axford et al. (1977), Drury and Völk (1981) and Axford et al. (1982) in order to account for the back reaction of the energetic particles on the flow. An alternative, nonlinear model that takes into account the energetic particle momentum spectrum and the modification of the flow by the energetic particles has been developed by Ellison (1981, 1985) (see the review by Jones and Ellison 1991).

Drury and Falle (1986) and Zank and McKenzie (1987) investigated in detail a short-wavelength instability for backward-propagating sound waves upstream of a cosmic-ray-modified shock, in which the gas density perturbations were amplified by the cosmic ray pressure gradient (see also Berezhko 1986; Chalov 1988; Webb 1989; Kang et al. 1992). McKenzie and Völk (1982) and Völk et al. (1984) developed an Alfvénic two-fluid model, in which the Alfvén waves scattering the cosmic rays and the cosmic-ray streaming instability were included as integral components. The cosmic-ray-generated Alfvén waves in this model were shown by McKenzie and Webb (1984), Zank (1989), Begelman and Zweibel (1994) and Ko and Jeng (1994) to drive one of the modified slow magneto-acoustic waves unstable. More general analyses of instabilities of obliquely propagating magnetosonic modes in cosmic-ray-modified flows have been investigated by Zank et al. (1990), who showed that the waves could be destabilized by squeezing and stratification effects and by particle drifts.

Webb et al. (1997a) considered the role of wave–wave interactions between the short-wavelength entropy wave and the backward and forward sound waves in cosmic-ray-modified flows and shocks in one Cartesian space dimension. In the linear wave regime, the waves are coupled via gradients in the large-scale background flow, and also by cosmic ray diffusive effects. The equations are similar in form to the wave mixing equations for Alfvén waves and Alfvénic turbulence in the solar wind (see e.g. Heinemann and Olbert 1980; Zhou and Matthaeus 1990). In the WKB limit, the waves are decoupled, and the equations reduce to those derived by Drury and Falle (1986) and Zank and McKenzie (1987) for WKB sound waves in cosmic ray shocks. Webb et al. (1997a) also considered weakly nonlinear wave interactions, namely the Burgers self wave interactions for sound waves and three-wave resonant interactions in which a sound wave is resonantly scattered off an entropy wave disturbance to produce a reverse sound wave.

The main aim of this paper is to investigate wave mixing and instabilities of short-wavelength waves in cosmic-ray-modified shocks by using the wave interaction equations for sound waves and entropy waves developed by Webb et al. (1997a,b,c). It is important at the outset to note the physical limitations of using a fluid-dynamical description, rather than a collisionless, kinetic plasma description (note that this criticism also applies to Monte Carlo models). In particular, the model does not incorporate Landau damping of magnetoacoustic modes due to wave particle interactions (see e.g. Barnes 1966, 1979). The damping rates $\gamma_L = -\Im(\omega)/\Re(\omega)$ (where ω is the wave frequency) of the magnetoacoustic waves in general increase with the plasma beta (see e.g. Fig. 4 of Barnes (1979), where γ_L is plotted as a function of the angle θ between the wave vector $\mathbf{k}$ and the background magnetic field $\mathbf{B}$ for the cases $\beta = 1$ and $\beta = 5$). The Landau damping for the fast-mode wave exhibits two peaks associated with stochastic heating of the thermal protons ($\theta \approx 10^\circ$) and heating of the electrons ($\theta \approx 85^\circ$–90°) in $\beta \approx 1$ plasmas. For perpendicular propagation ($\theta = 90^\circ$), there is no linear Landau damping of the fast mode (this corresponds to waves propagating normal to the shock in a perpendicular,

cosmic-ray-modified shock). In collisionless plasma theory, the entropy-wave-like modes with $\Re(\omega) = 0$ are Landau-damped (Barnes 1979). In general, it is difficult to assess whether the cosmic ray squeezing instability is sufficiently vigorous to overcome Landau damping, without carrying out detailed calculations. In a more complete theory, one should also take into account the full momentum spectrum of the cosmic rays, obtained by solving the cosmic ray transport equation (see e.g. Parker 1965) consistent with the total momentum equation for the system, in which the cosmic rays exert a force on the background flow via their pressure gradient. Further work on the wave mixing equations for the magnetohydrodynamic (MHD) wave modes in MHD models of cosmic-ray-modified shocks is described in Webb et al. (1999).

In Sec. 2, the equations for the two-fluid model are introduced. Section 3 discusses the wave mixing equations for short-wavelength waves in a non-uniform large-scale background flow. Section 4 considers the form of the wave interaction equations for the case of a uniform background flow. In this case, the backward and forward sound waves are coupled by cosmic ray interaction effects, via the parameter $\alpha = a_c^2/2\kappa$, where $a_c = (\gamma_c p_c/\rho)^{1/2}$ is the cosmic ray sound speed (p_c and γ_c denote the cosmic ray pressure and adiabatic index, and ρ denotes the density of the thermal gas), and κ is the hydrodynamical cosmic ray diffusion coefficient. Analytical solutions of the wave interaction equations are obtained corresponding to initial conditions in which the sound wave density perturbations consist of Dirac delta distributions. The solutions consist of decaying delta function pulses located on the backward *and/or* forward sound wave characteristics, plus a wake of particles trapped between the characteristics arising from wave–wave interactions. In Sec. 5, a WKB analysis of the Fourier-transformed wave mixing equations for the case of a steady non-uniform background flow is developed. Two methods are used. In the first, the WKB analysis is based on a differential equations approach, whereas in the second method, an integral equation formulation of the equations is used. WKB expansion of the iterated solutions of the integral equations are used to reveal the lowest-order correction to the WKB solutions due to wave mixing. Section 6 presents numerical solutions of the two-fluid equations illustrating the the role of wave mixing and instabilities in cosmic-ray-modified shocks and flows. Depending on the characteristics of the background flow, the waves may grow to nonlinear amplitudes (see also Webb et al. 1997a,c). We present calculations of wave interactions and instabilities in a non-uniform background flow (a) by using a spectral code to solve the wave mixing equations and (b) by solving the ordinary differential equations for waves of a single frequency in a steady non-uniform background flow (the differential equation system is also solved by iterating the equivalent integral equation system). The results obtained in (a) and (b) are compared with WKB results for high-frequency waves. Wave propagation problems in cosmic-ray-modified shocks and pressure balance structures are studied. Section 7 discusses the role of the cosmic ray squeezing instability and wave mixing in supernova remnant shocks propagating through the warm interstellar medium (WISM) and hot interstellar medium (HISM). Section 8 concludes with a summary and discussion.

2. The model and equations

The two-fluid model of cosmic-ray-modified flows and shocks (Axford et al. 1977, 1982; Drury and Völk 1981) was initially developed to describe the self-consistent

modification of astrophysical shocks by energetic particles accelerated at the shock by the first-order Fermi mechanism. The cosmic rays are assumed to be a hot low-density gas, with negligible mass flux. The cosmic rays are scattered by waves or turbulence in the background flow, and the phase velocity of the waves is assumed to be negligible compared with the fluid speed.

For the case of flows in one Cartesian space dimension, the two-fluid cosmic ray hydrodynamical equations may be written in the form

$$\frac{\partial \rho}{\partial t} + \frac{\partial}{\partial x}(\rho u) = 0, \tag{2.1}$$

$$\frac{\partial u}{\partial t} + u\frac{\partial u}{\partial x} = -\frac{1}{\rho}\left(\frac{\partial p_c}{\partial x} + \frac{\partial p_g}{\partial x}\right), \tag{2.2}$$

$$\frac{\partial p_g}{\partial t} + u\frac{\partial p_g}{\partial x} + \gamma_g p_g \frac{\partial u}{\partial x} = 0, \tag{2.3}$$

$$\frac{\partial p_c}{\partial t} + u\frac{\partial p_c}{\partial x} + \gamma_c p_c \frac{\partial u}{\partial x} - \frac{\partial}{\partial x}\left(\kappa \frac{\partial p_c}{\partial x}\right) = 0. \tag{2.4}$$

Here ρ, u, p_g, and γ_g denote the density, fluid velocity, pressure and adiabatic index for the thermal gas, and p_c, γ_c and κ denote the cosmic ray pressure, adiabatic index and hydrodynamical diffusion coefficient.

An alternative, equivalent set of equations for the model consists of the overall mass, momentum and energy equations for the two fluids, supplemented by the cosmic ray energy equation:

$$\frac{\partial}{\partial t}\left(\frac{p_c}{\gamma_c - 1}\right) + \frac{\partial}{\partial x}\left(\frac{\gamma_c p_c}{\gamma_c - 1}u - \frac{\kappa}{\gamma_c - 1}\frac{\partial p_c}{\partial x}\right) = u\frac{\partial p_c}{\partial x}, \tag{2.5}$$

which describes the interaction of the cosmic rays with the background flow (see e.g. Axford et al. 1977; Webb et al. 1997a). Equation (2.5) is derived by taking the kinetic energy moment of the cosmic ray transport equation obtained by Krymsky (1964), Parker (1965), Gleeson and Axford (1967) and Dolginov and Toptygin (1967), describing energetic-particle transport in the solar wind. Equation (2.5), which is equivalent to (2.4), shows that the background flow does work on the cosmic rays at the rate $u\partial p_c/\partial x$. The entropy advection equation

$$\frac{\partial S}{\partial t} + u\frac{\partial S}{\partial x} = 0, \tag{2.6}$$

is equivalent to the co-moving gas energy equation (2.3), where

$$S = C_v \ln\left(\frac{p_g}{\rho^{\gamma_g}}\right), \tag{2.7}$$

is the entropy of the thermal gas and C_v is the specific heat at constant volume. By making use of the mass continuity equation (2.3), the entropy equation may be cast in the conservative form

$$\frac{\partial}{\partial t}(\rho S) + \frac{\partial}{\partial x}(\rho u S) = 0. \tag{2.8}$$

Hence the entropy is advected with the flow, except at gas subshocks, where S jumps discontinuously. The entropy equation, (2.6) or (2.8), may be replaced by the total energy equation

$$\frac{\partial}{\partial t}\left(\tfrac{1}{2}\rho u^2 + \frac{p_g}{\gamma_g - 1} + \frac{p_c}{\gamma_c - 1}\right) + \frac{\partial}{\partial x}\left[\rho u\left(\tfrac{1}{2}u^2 + \frac{\gamma_g p_g}{(\gamma_g - 1)\rho}\right) + F_c\right] = 0, \tag{2.9}$$

https://doi.org/10.1017/S0022377898007466 Published online by Cambridge University Press

where

$$F_c = \frac{\gamma_c p_c}{\gamma_c - 1} u - \frac{\kappa}{\gamma_c - 1} \frac{\partial p_c}{\partial x}, \tag{2.10}$$

is the cosmic ray energy flux. Equations (2.1)–(2.4) may be combined with the total energy equation (2.9) to yield the entropy equation (2.6).

The cosmic rays may be scattered both by resonant wave–particle interactions, and by random walk of the field lines (see e.g., Jokipii 1971). The general form of the energetic particle diffusion coefficient k_{xx} in the kinetic transport equation for cosmic rays (see e.g. Krymsky 1964; Parker 1965) is of the form

$$k_{xx} = \kappa_{\parallel} \cos^2 \theta_{Bn} + \kappa_{\perp} \sin^2 \theta_{Bn}, \tag{2.11}$$

where $\kappa_{\parallel}$ and $\kappa_{\perp}$ are the particle diffusion coefficients parallel and perpendicular to the background magnetic field B, and θ_{Bn} is the angle between the background magnetic field and the x axis, or shock normal. The parallel diffusion coefficient $\kappa_{\parallel}$ is determined by resonant wave–particle interactions whereas the perpendicular diffusion coefficient $\kappa_{\perp}$ is determined both by resonant wave particle interactions, and by random walk of the field lines. For slab turbulence, in which the magnetic fluctuations are perpendicular to $\mathbf{B}$, $\kappa_{\perp}$ is determined by random walk of the field lines. In this case, one finds $\kappa_{\parallel} \propto 1/P_w$, where $P_w = (\delta B)^2/8\pi$ is the Alfvén wave pressure, whereas the perpendicular diffusion coefficient $\kappa_{\perp}$ is proportional to the power at zero frequency. The hydrodynamically averaged diffusion coefficient κ is an average of k_{xx} over the energetic particle momentum spectrum (see e.g. Drury and Völk 1981). Drury and Falle (1986) note that if resonant wave–particle interactions are the main scattering mechanism then the hydrodynamically averaged diffusion coefficient $\kappa \propto 1/P_w$. From the compression of pre-existing Alfvén waves, $P_w \propto \rho^{3/2}$, suggesting $\kappa \propto \rho^{-3/2}$ for the case where k_{xx} is dominated by $\kappa_{\parallel}$. However, Alfvén wave excitation by the resonant streaming instability will also contribute to P_w (see e.g. McKenzie and Völk 1982).

On the other hand, in a quasiperpendicular shock, $k_{xx} \approx \kappa_{\perp}$ ($\theta_{Bn} \approx \frac{1}{2}\pi$ in (2.11)). If $\kappa_{\perp}$ is dominated by random walk of the field lines (Jokipii 1971, equation (65)) one can show that $\kappa_{\perp} \propto (\delta B/B)^2$. From the wave mixing equations for Alfvén waves (see e.g. Zhou and Matthaeus 1990), one can show that $\delta B \propto \rho$ in a quasiperpendicular shock. Because both $\delta B \propto \rho$ and $B \propto \rho$, it follows that $\kappa \approx$ const in a quasiperpendicular shock. The present purely fluid-dynamical model strictly only applies to shocks in which the plasma β is sufficiently large that the background magnetic field plays no dynamical role.

These arguments suggest that

$$\kappa = \kappa(\rho) \tag{2.12}$$

is a function of the background density ρ. It turns out that the squeezing instability for short-wavelength sound waves in cosmic-ray modified shocks, first investigated in detail by Drury and Falle (1986), is sensitive to the form of $\kappa(\rho)$. More specifically, the squeezing instability depends on the value of the parameter

$$\zeta = \frac{\partial \ln \kappa}{\partial \ln \rho}. \tag{2.13}$$

The instability growth rate also depends on the cosmic ray pressure gradient, and is substantially enhanced for a low-temperature background thermal gas. This is discussed in further detail in the next section.

3. Short-wavelength waves in non-uniform flows

From Webb et al. (1997a), linear short-wavelength waves in the two-fluid model propagating through a non-uniform background medium satisfy linear wave evolution equations of the form

$$\frac{\partial \rho_i}{\partial t} + \frac{\partial}{\partial x}(\lambda_i \rho_i) + \sum_{j=1}^{3} \Lambda_{ij}\rho_j = 0, \quad i = 1,2,3, \tag{3.1}$$

where the $\{\rho_i : \ i = 1,2,3\}$ are the density perturbations for the backward sound wave (ρ_1), entropy wave (ρ_2) and forward sound wave (ρ_3) respectively. The phase speeds of the waves are

$$\lambda_1 = u - a_g, \qquad \lambda_2 = u, \qquad \lambda_3 = u + a_g, \tag{3.2}$$

where $a_g = (\gamma_g p_g/\rho)^{1/2}$ is the thermal gas sound speed. The density perturbations ρ_1, ρ_2 and ρ_3 may be expressed in terms of the perturbations ρ^1, u^1 and S^1 of the gas density, velocity and entropy, by the equations

$$\rho_1 = \frac{1}{2}\left(\rho^1 + \frac{\rho S^1}{\gamma_g C_v} - \frac{\rho u^1}{a_g}\right), \tag{3.3a}$$

$$\rho_2 = -\frac{\rho S^1}{\gamma_g C_v}, \tag{3.3b}$$

$$\rho_3 = \frac{1}{2}\left(\rho^1 + \frac{\rho S^1}{\gamma_g C_v} + \frac{\rho u^1}{a_g}\right). \tag{3.3c}$$

The velocity perturbations for the sound waves are $v_1 = -a_g\rho_1/\rho$ and $v_3 = a_g\rho_3/\rho$. The entropy wave has zero velocity perturbation. Note that $\rho^1 = \rho_1 + \rho_2 + \rho_3$ and $u^1 = a_g(\rho_3 - \rho_1)/\rho$.

In the applications of the wave mixing equations (3.1) to cosmic-ray-modified shocks (Secs 5–7), we adopt the convention that $x \to \infty$ far upstream ($x \to -\infty$ far downstream). In the upstream reference frame, $u \to 0$ as $x \to \infty$. The forward-propagating sound wave has velocity $\mathbf{V}_{p3} = (u + a_g)\mathbf{e}_x$ and propagates into the upstream medium away from the shock, whereas the backward sound wave in the upstream medium has phase velocity $\mathbf{V}_{p1} = (u - a_g)\mathbf{e}_x$ and propagates in the negative x direction towards the advancing shock.

The wave interaction coefficients depend on the gradients of the non-uniform background flow, and have the form

$$\Lambda_{11} = \frac{1}{2}\left(\frac{(3-\gamma_g)}{2}R_x^+ - \frac{a_g S_x}{(\gamma_g - 1)C_v} + \frac{a_c^2}{\kappa} + \frac{\zeta + 1}{\rho a_g}\frac{\partial p_c}{\partial x}\right), \tag{3.4a}$$

$$\Lambda_{12} = \frac{1}{2}\left(\frac{R_x^+ - R_x^-}{2} - \frac{a_g S_x}{\gamma_g(\gamma_g - 1)C_v} + \frac{\zeta + 1}{\rho a_g}\frac{\partial p_c}{\partial x}\right) \equiv -\frac{1}{2a_g}\frac{du}{dt} + \frac{\zeta}{2\rho a_g}\frac{\partial p_c}{\partial x}, \tag{3.4b}$$

$$\Lambda_{13} = \frac{1}{2}\left(\frac{\gamma_g - 3}{2}R_x^- + \frac{(\gamma_g - 2)a_g S_x}{\gamma_g(\gamma_g - 1)C_v} + \frac{\zeta + 1}{\rho a_g}\frac{\partial p_c}{\partial x} - \frac{a_c^2}{\kappa}\right), \tag{3.4c}$$

$$\Lambda_{21} = -\Lambda_{23} = \frac{a_g S_x}{\gamma_g C_v}, \tag{3.4d}$$

$$\Lambda_{22} = 0, \tag{3.4e}$$

$$\Lambda_{31} = \frac{1}{2}\left(\frac{\gamma_g - 3}{2}R_x^+ - \frac{(\gamma_g - 2)a_g S_x}{\gamma_g(\gamma_g - 1)C_v} - \frac{\zeta + 1}{\rho a_g}\frac{\partial p_c}{\partial x} - \frac{a_c^2}{\kappa}\right), \tag{3.4f}$$

https://doi.org/10.1017/S0022377898007466 Published online by Cambridge University Press

$$\Lambda_{32} = -\Lambda_{12}, \tag{3.4g}$$

$$\Lambda_{33} = \frac{1}{2}\left(\frac{3-\gamma_g}{2}R_x^- + \frac{a_g S_x}{(\gamma_g - 1)C_v} + \frac{a_c^2}{\kappa} - \frac{\zeta+1}{\rho a_g}\frac{\partial p_c}{\partial x}\right), \tag{3.4h}$$

where the parameter β is defined in (2.13), $du/dt = \partial u/\partial t + u\partial u/\partial x$ is the acceleration vector of the fluid and

$$R^{\pm} = u \pm \frac{2a_g}{\gamma_g - 1}, \tag{3.5}$$

are the Riemann invariants of isentropic gas dynamics. The coefficients $\{\Lambda_{3j}\colon j = 1, 2, 3\}$ for the forward sound wave are obtained by making the substitutions $1 \leftrightarrow 3$ and $a_g \leftrightarrow -a_g$ in the backward sound wave coefficients $\{\Lambda_{1j}\}$ (note that $R^- \leftrightarrow R^+$ under this transformation). The wave mixing coefficients $\{\Lambda_{ij}\}$ in (3.4) are slightly more general than those presented in Webb et al. (1997a,b,c) where the coefficients were given for the case of a constant diffusion coefficient with $\beta \equiv \partial \ln \kappa/\partial \ln \rho = 0$.

The terms involving $\partial p_c/\partial x$ in (3.4) correspond to the cosmic ray squeezing instability investigated by Dorfi and Drury (1985), Drury and Falle (1986) and Zank and McKenzie (1987). Note that the character of the instability depends on whether $\zeta < -1$, $\zeta = -1$ or $\zeta > -1$, where $\zeta = \partial \ln \kappa/\partial \ln \rho$. Note also that the squeezing instability terms are proportional to $(\partial p_c/\partial x)/\rho a_g$. Hence the instability is enhanced if $\partial p_c/\partial x$ is large or if the thermal gas temperature is small, so that a_g is small. The a_c^2/κ terms correspond to damping of the sound waves by the diffusing cosmic rays, where $a_c = (\gamma_c p_c/\rho)^{1/2}$ is the 'cosmic ray sound speed'.

Using (2.1)–(2.4), R^- and R^+ satisfy the equations

$$\frac{\partial R^-}{\partial t} + \lambda_1 \frac{\partial R^-}{\partial x} = \frac{\partial R^+}{\partial t} + \lambda_3 \frac{\partial R^+}{\partial x} = \frac{a_g^2}{\gamma_g(\gamma_g - 1)C_v}\frac{\partial S}{\partial x} - \frac{1}{\rho}\frac{\partial p_c}{\partial x}. \tag{3.6}$$

For isentropic gas flows (with no cosmic rays) the Riemann invariant R^- is constant on the backward sound wave characteristic, whereas R^+ is constant on the forward sound wave characteristic. In an R^+ simple wave background flow in the absence of cosmic rays $R^+ = $ const. and $S = $ const. and $\Lambda_{11} = \Lambda_{21} = \Lambda_{31} = 0$. An R^+ simple wave is a backward-moving nonlinear sound wave in which $du = -a_g d\rho/\rho$ and R^+ is constant. In such a flow, the backward linear sound perturbation does not interact with the other wave modes.

From the background flow equations (2.1)–(2.4) and the wave interaction equations (3.1), the linearized continuity equation and entropy flux equation may be written in the conservative forms

$$(\rho_1 + \rho_2 + \rho_3)_t + (\lambda_1\rho_1 + \lambda_2\rho_2 + \lambda_3\rho_3)_x = 0, \tag{3.7}$$

$$\left[S(\rho_1 + \rho_2 + \rho_3) - \gamma_g C_v \rho_2\right]_t + \left[S(\lambda_1\rho_1 + \lambda_2\rho_2 + \lambda_3\rho_3) - \gamma_g C_v \lambda_2 \rho_2\right]_x = 0, \tag{3.8}$$

where the subscripts x and t denote partial derivatives with respect to x and t. Similarly, the perturbed momentum equation may be written in the form

$$(\lambda_1\rho_1 + \lambda_2\rho_2 + \lambda_3\rho_3)_t + (\lambda_1^2\rho_1 + \lambda_2^2\rho_2 + \lambda_3^2\rho_3)_x = Q_P, \tag{3.9}$$

where

$$Q_P = \frac{\zeta}{\rho}\frac{\partial p_c}{\partial x}(\rho_1 + \rho_2 + \rho_3) - \rho\frac{a_c^2}{\kappa}(v_1 + v_3). \tag{3.10}$$

https://doi.org/10.1017/S0022377898007466 Published online by Cambridge University Press

The source Q_P in (3.9) and (3.10) consists of a squeezing instability term ($\propto \partial p_c/\partial x$) and a diffusive cosmic ray damping term ($\propto a_c^2/\kappa$), and corresponds to the short-scale terms in a multiple-scales analysis of (2.1)–(2.4). It is straightforward to write down the linearized total energy equation for the system, which in the gas dynamical case has a conservative form.

Discussions of the canonical wave energy equation and wave action equations associated with the wave mixing equations (3.1) are given in Webb et al. (1997a,b). Webb et al. (1998) consider the case of wave mixing in adiabatic gas dynamics in the absence of cosmic rays. In the latter paper, Lagrangian and Hamiltonian formulations of the wave mixing equations are developed, and the form of the canonical and physical stress energy tensors for the waves and the background flow are discussed.

In the following sections, we consider both analytical and approximate solutions of the wave mixing equations (3.1) (Secs 4 and 5). Numerical solutions of the two-fluid equations (2.1)–(2.4) and of the wave mixing equations (3.1) are explored in Sec. 6. Unless otherwise indicated, the analysis applies to the case of constant diffusion coefficient κ = const. Case (a) corresponds to the expected dependence of κ if the scattering wave field is due to pre-existing Alfvén waves upstream of a quasi-parallel shock. As noted in (3.5) et seq., there are two distinct behaviours expected for the cosmic ray squeezing instability, depending on the density dependence of $\kappa(\rho)$. In case (a), the forward-propagating sound wave upstream of a cosmic-ray-modified shock is driven unstable by the cosmic ray squeezing instability, whereas in case (b), the backward sound wave is driven unstable. Case (b) corresponds to a perpendicular shock configuration in which $\kappa_\perp$ is due to random walk of the field lines, and for which δB and B are both proportional to ρ (see the discussion following (2.11)).

4. Wave evolution equations for a uniform background state

For a uniform background state, the wave mixing equations (3.1) for the backward and forward sound waves reduce to

$$\frac{\partial \rho_1}{\partial t} + \lambda_1 \frac{\partial \rho_1}{\partial x} + \alpha(\rho_1 - \rho_3) = 0, \tag{4.1}$$

$$\frac{\partial \rho_3}{\partial t} + \lambda_3 \frac{\partial \rho_3}{\partial x} + \alpha(\rho_3 - \rho_1) = 0, \tag{4.2}$$

where

$$\alpha = \frac{a_c^2}{2\kappa} \tag{4.3}$$

is a characteristic frequency describing the coupling and damping of the sound waves. In this section, we consider the solution of the initial value problem for (4.1) and (4.2) in which

$$\rho_1(x,0) = N_1\delta(x), \qquad \rho_3(x,0) = N_3\delta(x), \tag{4.4}$$

and $|\rho_1| \to 0$, $|\rho_3| \to 0$ as $|x| \to \infty$. The solution of the initial value problem (4.1)–(4.4) is of interest in describing the coupling of the sound waves far upstream and far downstream of a cosmic-ray-modified shock, where the flow is uniform.

https://doi.org/10.1017/S0022377898007466 Published online by Cambridge University Press

The initial value problem (4.1)–(4.4) may be posed as an initial value problem in the fluid frame as

$$\frac{\partial \hat{\rho}_1}{\partial t} - a_g \frac{\partial \hat{\rho}_1}{\partial x'} = \alpha \hat{\rho}_3, \tag{4.5}$$

$$\frac{\partial \hat{\rho}_3}{\partial t} + a_g \frac{\partial \hat{\rho}_3}{\partial x'} = \alpha \hat{\rho}_1, \tag{4.6}$$

where

$$x' = x - ut, \qquad \hat{\rho}_1(x', t) = \exp(\alpha t)\, \rho_1(x, t), \qquad \hat{\rho}_3(x', t) = \exp(\alpha t)\, \rho_3(x, t), \tag{4.7}$$

and

$$\hat{\rho}_1(x', 0) = N_1 \delta(x'), \qquad \hat{\rho}_3(x', 0) = N_3 \delta(x'), \tag{4.8}$$

are the initial conditions. Substituting for $\hat{\rho}_3$ from (4.5) into (4.6) yields the Klein–Gordon-type equation

$$\frac{\partial^2 \hat{\rho}_1}{\partial t^2} - a_g^2 \frac{\partial^2 \hat{\rho}_1}{\partial x'^2} - \alpha^2 \hat{\rho}_1 = 0, \tag{4.9}$$

for $\hat{\rho}_1$. Exactly the same Klein–Gordon equation is satisfied by $\hat{\rho}_3$. Equations (4.5), (4.6) and (4.9) are similar to the idealized wave mixing equations for Alfvén waves in the solar wind, studied by Hollweg (1996).

The solution of the initial value problem (4.1)–(4.4) or (4.5)–(4.9) may be obtained by means of Laplace transforms (Appendix A). The solution for $\rho_1(x, t)$ is

$$\begin{aligned} \rho_1(x, t) = {} & N_1 \delta(x - x_1) \exp(-\alpha t) \\ & + \frac{\alpha \exp(-\alpha t)}{2 a_g} \left(N_1 \left| \frac{x_3 - x}{x - x_1} \right|^{1/2} I_1(z) + N_3 I_0(z) \right) \\ & \times [H(x - x_1) - H(x - x_3)], \end{aligned} \tag{4.10}$$

where

$$z = \frac{\alpha}{a_g} |(x - x_1)(x_3 - x)|^{1/2}, \tag{4.11}$$

$$x_1 = \lambda_1 t, \quad x_3 = \lambda_3 t. \tag{4.12}$$

The corresponding solution for $\rho_3(x, t)$ is

$$\begin{aligned} \rho_3(x, t) = {} & N_3 \delta(x - x_3) \exp(-\alpha t) \\ & + \frac{\alpha \exp(-\alpha t)}{2 a_g} \left[N_3 \left| \frac{x - x_1}{x_3 - x} \right|^{1/2} I_1(z) + N_1 I_0(z) \right] \\ & \times [H(x - x_1) - H(x - x_3)], \end{aligned} \tag{4.13}$$

where $I_0(z)$ and $I_1(z)$ are modified Bessel functions of orders 0 and 1, and $H(x)$ is the Heaviside step function. The solutions (4.11)–(4.13) for $\rho_1(x, t)$ and $\rho_3(x, t)$ apply for subsonic, sonic and supersonic flow.

Note that the solutions (4.10)–(4.13) are only non-zero between the sound wave characteristics $x = x_1$ and $x = x_3$. Figure 1 shows schematically the region between the backward and forward sound wave characteristics $t = x/\lambda_1$ and $t = x/\lambda_3$ where the solutions are non-zero, for the cases of (a) subsonic flow ($0 < M < 1$), (b) sonic flow ($M = 1$), and (c) supersonic flow ($M > 1$), where $M = u/a_g$ is the Mach number. The solutions (4.10) and (4.13) for $\rho_1(x, t)$ and $\rho_3(x, t)$ consist of delta function source terms located on the backward and forward sound wave characteristics,

https://doi.org/10.1017/S0022377898007466 Published online by Cambridge University Press

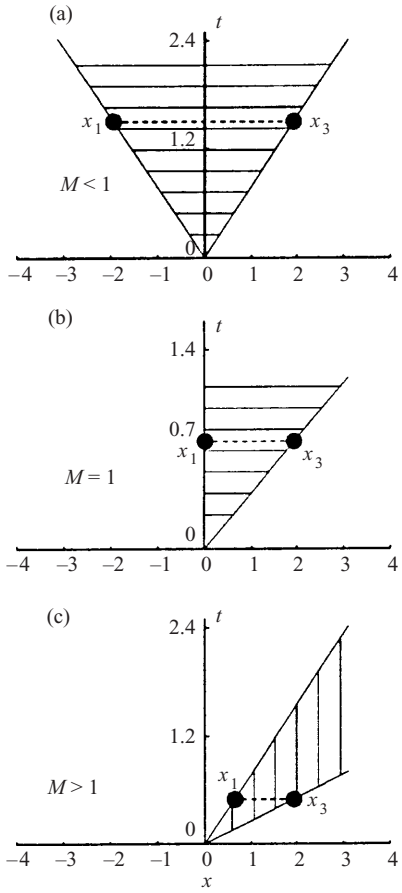

Figure 1. Schematic of the region between the backward and forward sound wave characteristics $t = t_1$ and $t = t_3$, where $t_1 = x/\lambda_1$ and $t_3 = x/\lambda_3$, for the cases of: (a) subsonic flow ($M < 1$); (b) sonic flow ($M = 1$) and (c) supersonic flow ($M > 1$). The Green-function solutions (4.9) and (4.12) are non-zero in the shaded regions.

which are exponentially damped, plus a diffusive wake of particles represented by the modified Bessel functions.

Figure 2 shows examples of the solutions (4.10) and (4.13) for ρ_1 and ρ_3 for a case where $\rho_1(x,0) = N_1\delta(x)$ and $\rho_3(x,0) = 0$. The parameters describing the background flow are $u = 0$, $\gamma_c = \frac{4}{3}$, $\gamma_g = \frac{5}{3}$, and $p_c = p_g = \rho = \kappa = 1$. For this set of parameters, $\alpha = \frac{2}{3}$ and $a_g = 1.291$. The solutions are shown at three time instants $t_1 = 0.4$, $t_2 = 1.2$ and $t_3 = 5.2$. The main point to note is that the solution for ρ_1 consists of an exponentially damped Dirac delta distribution pulse on the backward sound wave characteristic $x = x_1 = \lambda_1 t$ and a wake of particles extending between the characteristics $x = x_1$ and $x = x_3$. The solution for ρ_3 consists of a wake of particles extending between the characteristics. At early times $t = t_1$, the backward wave consists primarily of the delta function pulse, with a very small wake. The delta function pulse integral is represented by the height of the vertical line on the left of the ρ_1 profile. Note that the top hat pulse of particles in the forward wave wake, which has been produced by wave coupling, is substantially larger than the backward wave wake. At the intermediate time $t = t_2$, the backward

https://doi.org/10.1017/S0022377898007466 Published online by Cambridge University Press

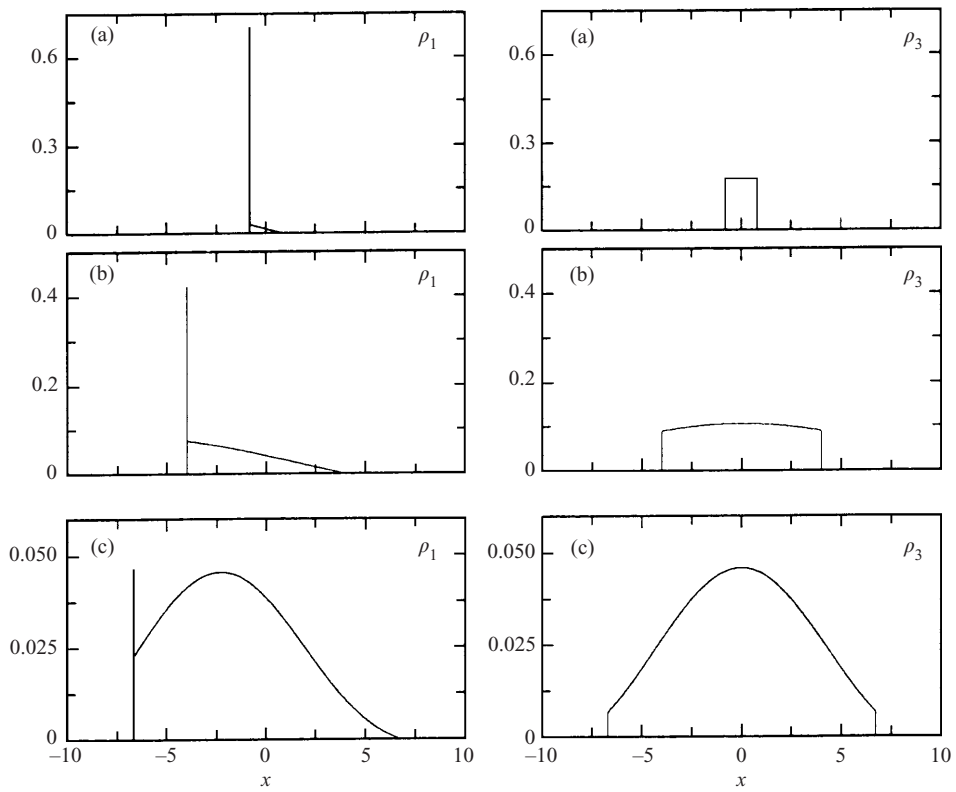

Figure 2. The Green-function solutions (4.9) and (4.12) describing the coupling of the backward (ρ_1) and forward (ρ_3) sound wave density perturbations for a uniform background flow. Initial conditions are $\rho_1(x,0) = N_1\delta(x)$ and $\rho_3(x,0) = 0$. The parameters used are $u = 0$, $\gamma_c = \frac{4}{3}$, $\gamma_g = \frac{5}{3}$, $p_c = p_g = \rho = \kappa = 1$. These values yield $\alpha = 0.667$ and $a_g = 1.291$. The density perturbations are shown at times (a) $t_1 = 0.4$, (b) $t_2 = 1.2$ and (c) $t_3 = 5.2$.

sound wave wake grows in amplitude, and becomes comparable in magnitude to the forward sound wave wake. Note the asymmetry in the backward wave wake. At late times $t = t_3$, the Dirac delta function representing the initial particles decreases exponentially with time t, and the two wakes dominate the solution. As $t \to \infty$, the two wakes become more similar, and approach the same bell-shaped profile.

5. WKB approaches to wave mixing

In this section, we develop a WKB analysis of the wave mixing equations applicable to steady background flows and cosmic-ray-modified shocks. We extend the work of Webb et al. (1997a) on WKB analyses of wave mixing in cosmic-ray-modified flows and shocks.

Section 5.1 considers the form of the wave mixing equations, for waves of a single frequency ω in a steady background flow. In Sec. 5.2, a WKB analysis of the wave mixing equations is developed based on a differential equations approach. In particular, we study the interaction of sound waves in a steady isentropic background flow, when there are no entropy waves present. We correct some errors in the analysis of Webb et al. (1997a), and provide a more exact matching procedure for the

https://doi.org/10.1017/S0022377898007466 Published online by Cambridge University Press

backward and forward sound waves. Section 5.3 considers an integral equation approach to wave mixing. Accurate solutions of the wave mixing equations may be obtained from the integral equations by iteration. One can also obtain approximate WKB solutions from the iterated solutions of the integral equations, which yield further insight into the effects of wave mixing. The integral equation approach has the virtue that initial value data and boundary data are automatically included in the integral equations, so that further analysis is not needed to ensure that the solutions for the different wave modes are properly meshed together. One defect of the integral equation approach to WKB expansions is that the Neumann expansion is non-uniform (Nayfeh 1973, Chap. 7), but this can, in principle, be remedied by renormalization techniques. In any event, the integral equation formulation leads to sufficiently accurate WKB expansions in a limited space domain, and yields physical insight into the wave mixing process. We compare the WKB expansions with accurate numerical solutions in Sec. 6.

We use the same normalized variables as Webb et al. (1997a). Length and time are normalized to characteristic length (L_1) and time (T_1) scales of the background flow, where $a_{g0} = L_1/T_1$ is a characteristic value of the gas sound speed. Velocities are normalized by a_{g0}, pressures are normalized by p_{g0}, the density is normalized by ρ_0, and the cosmic ray diffusion coefficient is normalized by $a_{g0}L_1$.

Two physical problems are studied in detail:

(a) the wave mixing of sound waves in a steady background flow, in the absence of entropy waves;

(b) the generation of sound waves by wave mixing arising from entropy waves initially present in the flow.

5.1. The wave mixing equations

From Webb et al. (1997a), the wave mixing equations (3.1) for steady, isentropic background flows may be reduced to the equations

$$\frac{\partial \rho_2}{\partial t} + \frac{\partial}{\partial x}(u\rho_2) = 0, \tag{5.1}$$

$$\frac{\partial f}{\partial t} + \lambda_1 \frac{\partial f}{\partial x} = \lambda_1(\nu_{11} f + \nu_{12}\rho_2 + \nu_{13} g), \tag{5.2}$$

$$\frac{\partial g}{\partial t} + \lambda_3 \frac{\partial g}{\partial x} = \lambda_3(\nu_{31} f + \nu_{32}\rho_2 + \nu_{33} g), \tag{5.3}$$

where the variables

$$f = \frac{\lambda_1 v_1}{(a_g/\rho)^{1/2}} \equiv -\lambda_1 \left(\frac{a_g}{\rho}\right)^{1/2} \rho_1,$$

$$g = \frac{\lambda_3 v_3}{(a_g/\rho)^{1/2}} \equiv \lambda_3 \left(\frac{a_g}{\rho}\right)^{1/2} \rho_3, \tag{5.4}$$

describe the backward (f) and forward (g) sound waves. In (5.1)–(5.3) the interaction coefficients $\{\nu_{ij}\}$ are given by

$$\nu_{11} = -\frac{1}{2\lambda_1}\left(\frac{a_c^2}{\kappa} + \frac{\zeta+1}{\rho a_g}\frac{\partial p_c}{\partial x}\right), \tag{5.5a}$$

$$\nu_{12} = \nu_{32} = -\frac{1}{2(a_g\rho)^{1/2}}\frac{du}{dt} \equiv -\frac{uu_x}{2(a_g\rho)^{1/2}}, \tag{5.5b}$$

https://doi.org/10.1017/S0022377898007466 Published online by Cambridge University Press

$$\nu_{33} = -\frac{1}{2\lambda_3}\left(\frac{a_c^2}{\kappa} - \frac{\zeta+1}{\rho a_g}\frac{\partial p_c}{\partial x}\right), \tag{5.5c}$$

$$\nu_{13} = \frac{\partial \psi}{\partial x} + \nu_{33}, \tag{5.5d}$$

$$\nu_{31} = \frac{\partial \psi}{\partial x} + \nu_{11}, \tag{5.5e}$$

$$\psi = -\tfrac{1}{2}\ln\left(\frac{a_g}{\rho}\right), \tag{5.5f}$$

and $\lambda_1 = u - a_g$, and $\lambda_3 = u + a_g$ denote the speeds of the backward and forward sound waves. For waves of a single frequency ω, (5.1)–(5.3) have solutions of the form

$$\eta = \Re\{\bar{\eta}\exp(-i\omega t)\}, \tag{5.6}$$

where $\Re\{z\}$ denotes the real part of the complex number z, and η represents a wave perturbation quantity (e.g. f, g, and ρ_2). Equations (5.1)–(5.3) in Fourier space reduce to

$$u\frac{d\bar{\rho}_2}{dx} + \left(\frac{du}{dx} - i\omega\right)\bar{\rho}_2 = 0, \tag{5.7}$$

$$\frac{d\bar{f}}{dx} - \left(\frac{i\omega}{\lambda_1} + \nu_{11}\right)\bar{f} = \nu_{12}\bar{\rho}_2 + \nu_{13}\bar{g}, \tag{5.8}$$

$$\frac{d\bar{g}}{dx} - \left(\frac{i\omega}{\lambda_3} + \nu_{33}\right)\bar{g} = \nu_{31}\bar{f} + \nu_{32}\bar{\rho}_2. \tag{5.9}$$

The entropy wave equation (5.7) has the explicit solution

$$\bar{\rho}_2(x,\omega) = \bar{\rho}_{20}(\omega)\frac{u_0}{u(x)}\exp(i\omega\phi_2), \qquad \phi_2 = \int_{x_0}^{x}\frac{dx'}{u(x')}. \tag{5.10}$$

Thus (5.7)–(5.9) reduce to two first-order differential equations (5.8) and (5.9) for the sound waves, in which the entropy wave solution $\bar{\rho}_2$ appears as a source term. Introducing auxiliary functions $\bar{F}(x,\omega)$ and $\bar{G}(x,\omega)$ for the backward and forward sound waves,

$$\bar{F}(x,\omega) = \bar{f}\exp(-i\omega\phi_1 - \gamma_1), \tag{5.11a}$$

$$\bar{G}(x,\omega) = \bar{g}\exp(-i\omega\phi_3 - \gamma_3), \tag{5.11b}$$

where

$$\phi_j = \int_{x_0}^{x}\frac{dx'}{\lambda_j}, \qquad \gamma_1 = \int_{x_0}^{x}\nu_{11}\,dx', \qquad \gamma_3 = \int_{x_0}^{x}\nu_{33}\,dx'. \tag{5.12}$$

and using the notation

$$\phi = \phi_3 - \phi_1, \qquad \gamma = \gamma_3 - \gamma_1, \tag{5.13}$$

(5.8) and (5.9) may be written in the form

$$\frac{d\bar{F}}{dx} = A\bar{G} + Q_1, \tag{5.14}$$

$$\frac{d\bar{G}}{dx} = B\bar{F} + Q_3, \tag{5.15}$$

where

$$A = \nu_{13}\exp(S), \qquad B = \nu_{31}\exp(-S), \qquad S = i\omega\phi + \gamma, \tag{5.16a}$$

https://doi.org/10.1017/S0022377898007466 Published online by Cambridge University Press

$$Q_1 = \nu_{12}\exp(-i\omega\phi_1 - \gamma_1)\bar{\rho}_2, \qquad Q_3 = \nu_{32}\exp(-i\omega\phi_3 - \gamma_3)\bar{\rho}_2. \tag{5.16b}$$

Equations (5.14) and (5.15) may be combined to yield second order differential equations for $\bar{F}$ and $\bar{G}$

$$\bar{F}_{xx} - D_x(\ln A)\bar{F}_x - AB\bar{F} = S_F, \tag{5.17}$$

$$\bar{G}_{xx} - D_x(\ln B)\bar{G}_x - AB\bar{G} = S_G, \tag{5.18}$$

where

$$S_F = Q_{1x} - D_x(\ln A)Q_1 + AQ_3, \tag{5.19a}$$

$$S_G = Q_{3x} - D_x(\ln B)Q_3 + BQ_1, \tag{5.19b}$$

are the source terms in (5.17) and (5.18). The source terms S_F and S_G depend on the presence of entropy waves in the flow. The second-order differential equations (5.17) and (5.18) formed the basis of the WKB analysis of wave mixing by Webb et al. (1997a). It is of interest to note that the differential equations (5.14) and (5.15) may be cast in Hamiltonian form, in which $\bar{F}$ and $\bar{G}$ are the canonical variables (Webb et al. 1997a).

5.2. WKB analysis: a differential equations approach

A standard WKB analysis of the second-order differential equations (5.17) and (5.18) for $\bar{F}$ and $\bar{G}$ was carried out by Webb et al. (1997a). Our main purpose is to provide a relatively accurate WKB formulation of wave mixing for high-frequency waves that improves upon the development of Webb et al. (1997a). We illustrate the method for the case of sound wave propagation in a steady background flow in the absence of entropy waves.

5.2.1. Sound waves in the absence of entropy waves. In the absence of entropy waves, (5.14) and (5.15) describing the backward and forward sound waves reduce to

$$\frac{d\bar{F}}{dx} = A\bar{G}, \tag{5.20a}$$

$$\frac{d\bar{G}}{dx} = B\bar{F}. \tag{5.20b}$$

Equations (5.20) may be combined to yield the homogeneous, second-order differential equations (5.17) and (5.18) with zero entropy wave source terms S_F and S_G. The homogeneous equations (5.17) and (5.18) have approximate WKB solutions of the form:

$$\bar{F} = \exp\left(\frac{1}{\epsilon}\sum_{n=0}^{\infty}\epsilon^n S_n\right), \tag{5.21a}$$

$$\bar{G} = \exp\left(\frac{1}{\epsilon}\sum_{n=0}^{\infty}\epsilon^n T_n\right), \tag{5.21b}$$

where, for high-frequency waves, the perturbation parameter $\epsilon = 1/\omega$. Substitution of the expansions (5.21) into the homogeneous forms of (5.17) and (5.18), and equating powers of ϵ, yields a set of ordinary differential equations for the $\{S_n\}$ and $\{T_n\}$. Some typographical errors in the equations for the $\{S_n\}$ presented in Webb et al. (1997a) are pointed out in Appendix B.

https://doi.org/10.1017/S0022377898007466 Published online by Cambridge University Press

The general solution of the homogeneous differential equations (5.17) and (5.18) for $\bar{F}$ and $\bar{G}$ may be written as

$$\bar{F} = c_1\bar{F}_1(x,\omega) + c_2\bar{F}_2(x,\omega), \tag{5.22a}$$

$$\bar{G} = d_1\bar{G}_1(x,\omega) + d_2\bar{G}_2(x,\omega). \tag{5.22b}$$

Approximate WKB solutions for $\bar{F}_1$ and $\bar{F}_2$, from Webb et al. (1997a), are

$$\bar{F}_1(x,\omega) = \exp\left(\frac{i}{\omega}\int_{x_0}^{x}\frac{\nu_{13}(y)\nu_{31}(y)}{\phi_y}dy + \frac{1}{\omega^2}\int_{x_0}^{x}\frac{\nu_{13}(y)\nu_{31}(y)}{\phi_y^2}\mu_{31}'(y)dy + \cdots\right), \tag{5.23}$$

$$\begin{aligned}\bar{F}_2(x,\omega) = \exp\Bigg\{ & i\omega\phi + \mu_{13}(x) - \mu_{13}(x_0) \\ & + \frac{i}{\omega}\left(\frac{\mu_{13}'(x)}{\phi_x} - \frac{\mu_{13}'(x_0)}{\phi_x(x_0)} - \int_{x_0}^{x}\frac{\nu_{13}(y)\nu_{31}(y)}{\phi_y}\,dy\right) \\ & + \frac{1}{\omega^2}\left(\left[\frac{\nu_{13}(y)\nu_{31}(y)}{\phi_y^2} - \frac{1}{2}\left(\frac{\mu_{13}'(y)}{\phi_y}\right)^2 - \frac{1}{\phi_y}D_y\left(\frac{\mu_{13}(y)}{\phi_y}\right)\right]_{y=x_0}^{y=x} \right. \\ & \left. + \int_{x_0}^{x}\frac{\nu_{13}(y)\nu_{31}(y)}{\phi_y^2}\mu_{13}'(y)dy\right) + \cdots\Bigg\},\end{aligned} \tag{5.24}$$

where

$$\mu_{13} = \ln\left[\frac{\nu_{13}}{\phi_x}\exp(\gamma)\right], \qquad \mu_{31} = \ln\left[\frac{\nu_{31}}{\phi_x}\exp(-\gamma)\right], \tag{5.25}$$

and the primed superscripts on $\mu_{13}(x)$ and $\mu_{31}(x)$ in (5.23) and (5.24) denote derivatives with respect to x. The operator D_y in (5.24) denotes differentiation with respect to y. Similarly, the approximate WKB solutions for $\bar{G}_1(x,\omega)$ and $\bar{G}_2(x,\omega)$ are given by the formulae

$$\bar{G}_1(x,\omega) = \exp\left(-\frac{i}{\omega}\int_{x_0}^{x}\frac{\nu_{13}(y)\nu_{31}(y)}{\phi_y}\,dy + \frac{1}{\omega^2}\int_{x_0}^{x}\frac{\nu_{13}(y)\nu_{31}(y)}{\phi_y^2}\mu_{13}'(y)dy + \cdots\right), \tag{5.26}$$

$$\begin{aligned}\bar{G}_2(x,\omega) = \exp\Bigg\{ & -i\omega\phi + \mu_{31}(x) - \mu_{31}(x_0) \\ & + \frac{i}{\omega}\left(\frac{\mu_{31}'(x_0)}{\phi_x(x_0)} - \frac{\mu_{31}'(x)}{\phi_x} + \int_{x_0}^{x}\frac{\nu_{13}(y)\nu_{31}(y)}{\phi_y}\,dy\right) \\ & + \frac{1}{\omega^2}\left(\left[\frac{\nu_{13}(y)\nu_{31}(y)}{\phi_y^2} - \frac{1}{2}\left(\frac{\mu_{31}'(y)}{\phi_y}\right)^2 - \frac{1}{\phi_y}D_y\left(\frac{\mu_{31}(y)}{\phi_y}\right)\right]_{y=x_0}^{y=x} \right. \\ & \left. + \int_{x_0}^{x}\frac{\nu_{13}(y)\nu_{31}(y)}{\phi_y^2}\mu_{31}'(y)dy\right) + \cdots\Bigg\}.\end{aligned} \tag{5.27}$$

Note that the formulae for $\bar{G}_1$ and $\bar{G}_2$ in (5.26) and (5.27) may be obtained from the formulae (5.23) and (5.24) for $\bar{F}_1$ and $\bar{F}_2$ by making the replacements $\phi \to -\phi$ and $1 \leftrightarrow 3$.

https://doi.org/10.1017/S0022377898007466 Published online by Cambridge University Press

Now consider solutions for $\bar{F}$ and $\bar{G}$ of (5.20), satisfying the initial conditions

$$\bar{F}(x_0) = \bar{F}_0, \qquad \bar{G}(x_0) = \bar{G}_0, \tag{5.28}$$

at $x = x_0$. This is equivalent to finding the constants c_1, c_2, d_1 and d_2 that ensure $\bar{F}$ and $\bar{G}$ satisfy the coupled first-order differential equations (5.20) and the initial conditions (5.28). One can obtain the required solution for $\bar{F}$ by solving the equivalent initial value problem for $\bar{F}$ in which $\bar{F}(x_0) = \bar{F}_0$, and $\bar{F}'(x_0) = \bar{F}_0'$ at $x = x_0$ where $\bar{F}_0' \equiv A_0\bar{G}_0$ and $A_0 \equiv A(x_0)$. In this way, we find

$$c_1 = \frac{W(\bar{F}_2, \bar{F})_0}{W(\bar{F}_2, \bar{F}_1)_0}, \qquad c_2 = \frac{W(\bar{F}_1, \bar{F})_0}{W(\bar{F}_2, \bar{F}_1)_0}, \tag{5.29a}$$

$$d_1 = \frac{W(\bar{G}_2, \bar{G})_0}{W(\bar{G}_2, \bar{G}_1)_0}, \qquad d_2 = \frac{W(\bar{G}_1, \bar{G})_0}{W(\bar{G}_2, \bar{G}_1)_0}, \tag{5.29b}$$

where

$$W(y_1, y_2) = y_1 y_2' - y_2 y_1' \tag{5.30}$$

denotes the Wronskian of $y_1(x)$ and $y_2(x)$, and the subscript 0 in (5.29) denotes evaluation at $x = x_0$.

Using the results (5.29) and (5.30) in (5.22) yields the WKB solutions

$$\begin{aligned}\bar{F} = {} & \frac{\bar{F}_0}{W(\bar{F}_2, \bar{F}_1)_0}[\bar{F}_{10}'\bar{F}_2(x,\omega) - \bar{F}_{20}'\bar{F}_1(x,\omega)] \\ & + \frac{A_0\bar{G}_0}{W(\bar{F}_2, \bar{F}_1)_0}[\bar{F}_{20}\bar{F}_1(x,\omega) - \bar{F}_{10}\bar{F}_2(x,\omega)],\end{aligned} \tag{5.31}$$

$$\begin{aligned}\bar{G} = {} & \frac{\bar{G}_0}{W(\bar{G}_2, \bar{G}_1)_0}[\bar{G}_{10}'\bar{G}_2(x,\omega) - \bar{G}_{20}'\bar{G}_1(x,\omega)] \\ & + \frac{B_0\bar{F}_0}{W(\bar{G}_2, \bar{G}_1)_0}[\bar{G}_{20}\bar{G}_1(x,\omega) - \bar{G}_{10}\bar{G}_2(x,\omega)]\end{aligned} \tag{5.32}$$

for $\bar{F}$ and $\bar{G}$. Note that the parameters $A_0 = A(x_0) \equiv \nu_{13}(x_0)$ and $B_0 = \nu_{31}(x_0)$ in (5.31) and (5.32) describe the coupling of the backward and forward sound waves. Using the transformations (5.4) and (5.11), the solutions for ρ_1 and ρ_3, for a single-frequency wave, are given by the equations

$$\rho_1 = -\frac{\Re\{\exp[i\omega(\phi_1 - t) + \gamma_1]\bar{F}\}}{(a_g/\rho)^{1/2}\lambda_1}, \tag{5.33a}$$

$$\rho_3 = \frac{\Re\{\exp[i\omega(\phi - t) + \gamma_3]\bar{G}\}}{(a_g/\rho)^{\frac{1}{2}}\lambda_3}, \tag{5.33b}$$

where $\bar{F}$ and $\bar{G}$ are given by (5.31) and (5.32). The results (5.31)–(5.33) are useful in determining fairly accurate WKB solutions (see Sec. 6). In the next subsection, we consider an integral equation approach to WKB expansions that yields more physically revealing, results than (5.31)–(5.33).

5.3. Wave mixing integral equations and WKB analysis

An alternative WKB analysis of the Fourier-space wave mixing equations (5.14)–(5.19) may be developed from an integral equation formulation of the equations. The WKB solutions are obtained from taking the high-frequency limit of the iterated solutions of the integral equations. We are interested in obtaining approximate

https://doi.org/10.1017/S0022377898007466 Published online by Cambridge University Press

WKB solutions of the initial value problem for (5.14) and (5.15) for which $\bar{F} = \bar{F}_0$ and $\bar{G} = \bar{G}_0$ at $x = x_0$.

5.3.1. Integral equations. By directly integrating (5.14) and (5.15) from $x' = x_0$ to $x' = x$, we obtain the integral equations

$$\bar{F}(x,\omega) = \bar{F}^0(x,\omega) + \int_{x_0}^{x} dy \int_{x_0}^{y} dz\ K(y,z)\bar{F}(z,\omega), \tag{5.34}$$

$$\bar{G}(x,\omega) = \bar{G}^0(x,\omega) + \int_{x_0}^{x} dy \int_{x_0}^{y} dz\ K(z,y)\bar{G}(z,\omega), \tag{5.35}$$

where

$$K(y,z) = A(y)B(z), \tag{5.36}$$

$$\bar{F}^0(x,\omega) = \bar{F}_0 + \bar{G}_0 \int_{x_0}^{x} dy\, A(y) + \int_{x_0}^{x} dy\, Q_1(y) + \int_{x_0}^{x} dy \int_{x_0}^{y} dz\ A(y)Q_3(z), \tag{5.37}$$

$$\bar{G}^0(x,\omega) = \bar{G}_0 + \bar{F}_0 \int_{x_0}^{x} dy\, B(y) + \int_{x_0}^{x} dy\, Q_3(y) + \int_{x_0}^{x} dy \int_{x_0}^{y} dz\ B(y)Q_1(z). \tag{5.38}$$

The integral equations (5.34)–(5.35) may be solved by iteration:

$$\bar{F}^{j+1} = \bar{F}^0 + \int_{x_0}^{x} dy \int_{x_0}^{y} dz\ K(y,z)\bar{F}^j(z,\omega), \tag{5.39}$$

$$\bar{G}^{j+1} = \bar{G}^0 + \int_{x_0}^{x} dy \int_{x_0}^{y} dz\ K(z,y)\bar{G}^j(z,\omega), \tag{5.40}$$

where $j = 0, 1, 2, \ldots$, etc., yielding the Neumann series for the integral equations. To obtain the lowest order WKB solutions, we use the solutions for F^1 and G^1, namely

$$\bar{F}^1 = \bar{F}^0(x,\omega) + \int_{x_0}^{x} dy \int_{x_0}^{y} dz\ K(y,z)\bar{F}^0(z,\omega), \tag{5.41}$$

$$\bar{G}^1 = \bar{G}^0(x,\omega) + \int_{x_0}^{x} dy \int_{x_0}^{y} dz\ K(z,y)\bar{G}^0(z,\omega), \tag{5.42}$$

where $\bar{F}^0$ and $\bar{G}^0$ are given by (5.37) and (5.38). In the high-frequency limit, integration by parts in the solutions for $\bar{F}^1$ and $\bar{G}^1$ yields the desired approximate solutions. Alternative sets of integral equations describing the system are discussed in Appendix C.

5.3.2. Wave mixing of sound waves in the absence of entropy waves. In the absence of entropy waves, $Q_1 = Q_3 = 0$ in the approximate solutions (5.41) and (5.42) for F and G. One can use the approximate integral equation solutions (5.41) and (5.42) to determine high-frequency solutions for $\bar{F}$ and $\bar{G}$. Use of the transformations (5.4) and (5.11) then yields high-frequency solutions for ρ_1 and ρ_3 in (x,t) space in the form

$$\rho_1 = -\frac{1}{\lambda_1(a_g/\rho)^{1/2}} \Re\left\{ \bar{F}_0 \exp[-i\omega(t-\phi_1)+\gamma_1] \left(1 + \frac{i}{\omega}\int_{x_0}^{x} dy\, \frac{\nu_{13}(y)\nu_{31}(y)}{\phi_y} dy\right) \right.$$
$$\left. -\frac{i\bar{G}_0}{\omega}\left(\frac{\nu_{13}(x)}{\phi_x}\exp[-i\omega(t-\phi_3)+\gamma_3] - \frac{\nu_{13}(x_0)}{\phi_x(x_0)}\exp[-i\omega(t-\phi_1)+\gamma_1]\right)\right\}, \tag{5.43}$$

https://doi.org/10.1017/S0022377898007466 Published online by Cambridge University Press

$$\rho_3 = \frac{1}{\lambda_3(a_g/\rho)^{1/2}}\Re\left\{\bar{G}_0\exp[-i\omega(t-\phi_3)+\gamma_3]\left(1-\frac{i}{\omega}\int_{x_0}^{x}dy\,\frac{\nu_{13}(y)\nu_{31}(y)}{\phi_y}\right)\right.$$
$$\left.+i\frac{\bar{F}_0}{\omega}\left(\frac{\nu_{31}(x)}{\phi_x}\exp[-i\omega(t-\phi_1)+\gamma_1]-\frac{\nu_{31}(x_0)}{\phi_x(x_0)}\exp[-i\omega(t-\phi_3)+\gamma_3]\right)\right\}. \quad (5.44)$$

If, for example, $F_0 = 1$ and $G_0 = 0$ then the solution (5.43) may be regarded as the primary wave, and the solution (5.44) for ρ_3 represents the generated wave. Note, however, that both ρ_1 and ρ_3 have generated wave components, which have amplitude $O(1/\omega)$ that of the primary wave. Near $x = x_0$, the solution for ρ_3 has a phase shift of approximately $-\frac{1}{2}\pi$ relative to that of the primary wave solution for ρ_1. The above solutions consist of a primary wave, plus wakes produced by wave–wave interactions, which is reminiscent of the solutions (4.9)–(4.12) of Sec. 4 with Dirac delta initial conditions.

5.3.3. Sound waves generated from entropy waves. In the absence of entropy waves, $F_0 = G_0$ in the approximate solutions (5.41) and (5.42) for $\bar{F}^1$ and $\bar{G}^1$. Taking the high-frequency approximation of (5.41) and (5.42) and using the results (5.4)–(5.11), we obtain

$$\rho_1 = -\Re\left\{\frac{i}{\omega}\frac{\bar{\rho}_{20}(\omega)u_0}{2\lambda_1(a_g/\rho)^{1/2}}\left(\nu_{12}(x)\frac{\lambda_1}{a_g}\exp[-i\omega(t-\phi_2)]\right.\right.$$
$$\left.\left.-\nu_{12}(x_0)\frac{\lambda_1(x_0)}{a_g(x_0)}\exp[-i\omega(t-\phi_1)+\gamma_1]\right)\right\}, \quad (5.45)$$

$$\rho_3 = -\Re\left\{\frac{i}{\omega}\frac{\bar{\rho}_{20}(\omega)u_0}{2\lambda_3(a_g/\rho)^{1/2}}\left(\nu_{32}(x)\frac{\lambda_3}{a_g}\exp[-i\omega(t-\phi_2)]\right.\right.$$
$$\left.\left.-\nu_{32}(x_0)\frac{\lambda_3(x_0)}{a_g(x_0)}\exp[-i\omega(t-\phi_3)+\gamma_3]\right)\right\}, \quad (5.46)$$

for the generated backward and forward sound wave density perturbations. The primary entropy wave has the density perturbation

$$\rho_2 = \frac{u_0}{u(x)}\Re\{\bar{\rho}_{20}(\omega)\exp[-i\omega(t-\phi_2)]\}. \quad (5.47)$$

Note that $\rho_1 = \rho_3 = 0$ at $x = x_0$. Note that the the solution for ρ_1, for example, consists of an exponential term that has the same phase as the entropy wave, plus a further term that has the phase one would expect for a backward sound wave. The density perturbations ρ_1 and ρ_3 in (5.45) and (5.46) have amplitudes that are $O(1/\omega)$ that of the primary entropy wave in (5.47). Alternative formulae for the generation of sound waves from entropy waves were derived in Webb et al. (1997a); these were based on WKB solutions of the differential equations (5.17) and (5.18). These latter formulae show that the generated sound waves consist of integrals over entropy wave source terms, in which the phase of the generated waves are $\pm\frac{1}{2}\pi$ out of phase with the entropy wave source at the point of generation, with characteristic change in the wave phase and amplitude between the generation, and observation points.

6. Numerical examples

In this section, we present numerical examples of the interaction of short-wavelength sound waves and entropy waves in cosmic-ray-modified flows. The

https://doi.org/10.1017/S0022377898007466 Published online by Cambridge University Press

main emphasis is on wave mixing and instabilities in cosmic-ray-modified shocks (Sec. 6.1). We compare spectral code solutions of the linear wave mixing equations (3.1), with fully nonlinear solutions of the two-fluid model equations (2.1)–(2.4) with the same initial conditions. The numerical and spectral code solutions are also compared with the WKB solution results of Sec. 5. It is important to note that the linear wave mixing equations (3.1) do not contain the effects of nonlinear wave interactions. Webb et al. (1997a) derived weakly nonlinear versions of the wave mixing equations (3.1), which contain further nonlinear terms describing (a) Burgers self-wave steepening terms for the sound waves, (b) mean wave field interaction terms, and (c) three-wave resonant interaction terms in which a sound wave resonantly interacts with an entropy wave to produce a reverse sound wave, provided the conditions for three-wave resonant interactions are satisfied. Section 6.2 considers wave propagation in cosmic-ray-modified pressure balance structures of the type considered by Webb et al. (1995). Cosmic ray pressure balance structures were also obtained in the numerical simulations of Donohue and Zank (1993) of the interaction of an interplanetary travelling shock with the solar wind termination shock.

6.1. Waves in cosmic-ray-modified shocks

6.1.1. Numerical simulations. In this subsection, we present numerical solutions of the nonlinear two-fluid equations (2.1)–(2.4) that illustrate wave interactions and instabilities in cosmic-ray-modified shocks. The basic strategy in solving the initial value problem for the time-dependent equations (2.1)–(2.4) consists of two steps:

(a) solve the cosmic ray energy equation (2.4) for p_c for a given flow velocity profile (for example by using a Crank–Nicholson scheme, or by using an explicit scheme with subcycling);

(b) solve (2.1)–(2.3) using a fluid code, such as Zeus 2D, suitably modified by the inclusion of an extra force term in the fluid momentum equation (2.2) due to the cosmic ray pressure gradient.

Figure 3 shows sample calculations of the density perturbations for sound waves and entropy waves in a smoothed cosmic-ray-modified shock. The diffusion coefficient in Fig. 3 has the form

$$\kappa = \kappa_0 \left(\frac{\rho}{\rho_0} \right)^{-3/2}, \tag{6.1}$$

where the subscript 0 denotes the values of physical quantities far upstream. This corresponds to the expected dependence of κ arising from the compression of a pre-existing Alfvén wave field upstream of a quasiparallel shock (see also (3.10) et seq.). In the left panels, a backward sound wave (ρ_1) is initially specified far upstream. To ensure that the initial data for the wave corresponds to a backward-propagating sound wave, the thermal gas pressure variations are specified using the isentropic form of the adiabatic gas law, and requiring that the velocity and density variations u^1 and ρ^1 satisfy the appropriate eigenrelation $\rho^1 = -\rho u^1/a_g$. The initial amplitude of the velocity fluctuations is taken to be one-tenth of the sound speed. The distance x is measured in units of the diffusion length scale κ_0/u_0. As initial conditions for the background flow we used a steady-state shock structure profile obtained by integrating the steady-state shock structure equation (see e.g. Axford et al. 1982), in which the upstream long-wavelength Mach number

https://doi.org/10.1017/S0022377898007466 Published online by Cambridge University Press

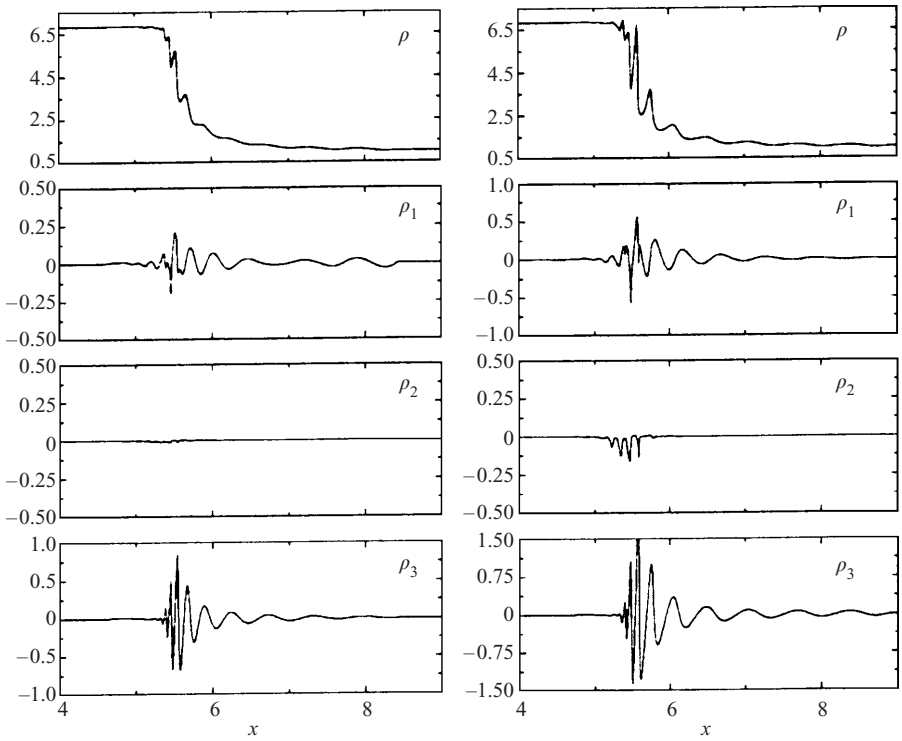

Figure 3. The density perturbations for the backward (ρ_1), and forward (ρ_3) sound waves and entropy wave (ρ_2) in a smooth, steady-state, cosmic-ray-modified shock. In the left panels, a backward sound wave is initially incident upon the shock from far upstream, whereas in the right panels, a forward sound wave is initially incident. The upstream long-wavelength Mach number $M_{l0} = 18.26$ and $p_{c0}/p_{g0} = 1$ as $x \to \infty$. The diffusion coefficient $\kappa = \kappa_0(\rho/\rho_0)^{-3/2}$, where $\kappa_0 = \text{const}$ (in computational units, $\kappa_0 = 1$). The density profile ρ and the perturbations ρ_1, ρ_2 and ρ_3 are shown at time $t = 10\kappa_0/u_0^2$.

$M_{l0} = u_0/(a_{g0}^2+a_{c0}^2)^{1/2} = 18.26$, and $p_{c0}/p_{g0} = 1.0$ and $\kappa_0 = 1$ far upstream ($x \to \infty$). The adiabatic indices for the cosmic rays and the thermal gas are taken as $\gamma_c = \frac{4}{3}$ and $\gamma_g = \frac{5}{3}$. The figure shows a snapshot of the density profile ρ and the density perturbations ρ_1, ρ_2 and ρ_3 at time $t = 10\tau_d$, where $\tau_d = \kappa_0/u_0^2$ is the diffusion time scale.

The initial backward-propagating sound wave (ρ_1) is damped (left panels of Fig. 3), but in the process generates the forward sound wave (ρ_3) via wave coupling. As the sound waves enter the shock precursor, the forward wave undergoes substantial growth, and regenerates the backward wave. Pure WKB theory would predict damping of ρ_1 with no coupling to ρ_3 and ρ_2. In the present linear theory, the entropy waves are generated only if there is a non-zero background entropy gradient S_x (note that S_x is zero for the steady-state smooth shock transition used in the initial conditions for the background flow).

The right panels of Fig. 3 show the evolution of the waves when the forward sound wave (ρ_3) is initially specified far upstream of the shock. The forward sound wave is driven unstable owing to the cosmic ray squeezing instability. Wave coupling leads to the generation of the backward sound wave. The amplitude of the forward wave in the middle of the shock ($x \approx 5.5$) is about three times that of the backward sound

https://doi.org/10.1017/S0022377898007466 Published online by Cambridge University Press

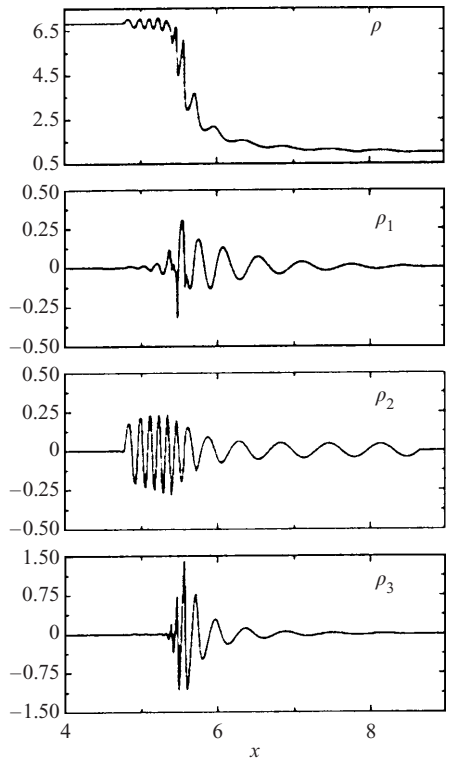

Figure 4. The density perturbations for the backward and forward sound waves (ρ_1 and ρ_3) and entropy wave (ρ_2) for the smoothed cosmic-ray-modified shock of Fig. 3, for the case where an entropy wave is initially specified upstream of the shock. The diffusion coefficient is the same as in Fig. 3.

wave. The generation of the entropy wave occurs in the region where the cosmic ray pressure gradient is large ($x \approx 5.5$), and the sound waves become nonlinear.

The entropy waves in Fig. 3 are only generated when the backward sound wave becomes sufficiently large in amplitude, suggesting that entropy waves are generated when the sound waves steepen into shocklets, or are generated by nonlinear coupling effects (Webb et al. 1997a). Substantially larger wave growth occurs for the case where only forward sound waves are initially present (right panels of Fig. 3) than for the case of backward sound wave initial conditions (left panels in Fig. 3). Far downstream, the large pressure of the accelerated cosmic rays and large damping rate $a_c^2/2\kappa$ leads to an effective quenching of the waves.

Figure 4 shows the corresponding results when only entropy waves are initially present. Both backward and forward sound waves are generated via wave mixing. As the waves progress through the shock, the sound waves grow owing to the the cosmic ray squeezing instability for the forward sound wave, and owing to wave coupling. The sound waves are strongly damped owing to the large damping rate $a_c^2/2\kappa$, far downstream. The WKB expansion results (5.45)–(5.47) for ρ_1, ρ_3 and ρ_2 indicate that the entropy wave generates both the backward and forward sound waves, but the entropy wave in turn is not affected by the sound waves because the coupling coefficients, which depend on S_x, are zero (see the shock precursor region $x \geqslant 7$). Further up the shock ramp ($x \leqslant 7$), entropy waves are gener-

https://doi.org/10.1017/S0022377898007466 Published online by Cambridge University Press

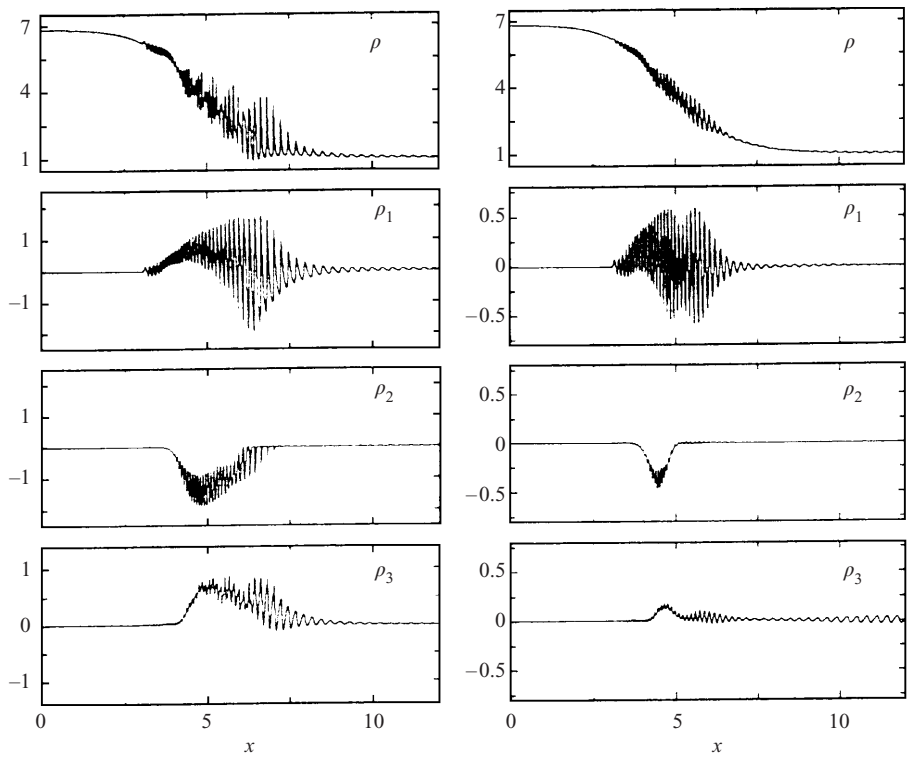

Figure 5. The density perturbations for the backward and forward sound waves (ρ_1 and ρ_3) and the entropy wave (ρ_2) in a smooth, steady-state, cosmic-ray-modified shock. The upstream long-wavelength Mach number $M_{l0} = 18.26$, $p_{c0}/p_{g0} = 1$ as $x \to \infty$, and $\kappa = \kappa_0 = 1$. In the left panels, a backward sound wave is initially incident upon the shock from far upstream, whereas a forward sound wave is initially incident in the right panels. The profiles are shown at time $t = 10\kappa_0/u_0^2$.

ated when the sound waves become nonlinear and shock-up. The forward sound wave profile ρ_3 has a larger amplitude than the the backward sound wave (ρ_1). The form of ρ_1 in (5.45) consists of two components: a component that has phase $-i\omega(t - \phi_2)$ characteristic of structures advected with the fluid, plus a further component with phase $-i\omega(t - \phi_1)$ corresponding to the backward sound wave with spatial growth rate γ_1. The solution (5.46) for ρ_3 has a similar structure consisting of an advected component plus a further component with the phase of the forward sound wave.

Figures 5 and 6 show similar examples of the interaction of sound waves and entropy waves with a cosmic-ray-ray modified shock with the same upstream conditions as in Figs 3 and 4, except that the hydrodynamical diffusion coefficient

$$\kappa = \kappa_0, \tag{6.2}$$

is taken to be constant throughout the shock structure ($\kappa_0 = 1$ in the units used in the computations). A constant value of κ is consistent with a perpendicular, cosmic-ray-modified shock configuration, in which particle diffusion across the magnetic field is due to random walk of the field lines (see Jokipii (1971) and the discussions following (2.11) and (3.10)). The left (right) panels of Fig. 5 correspond to the case

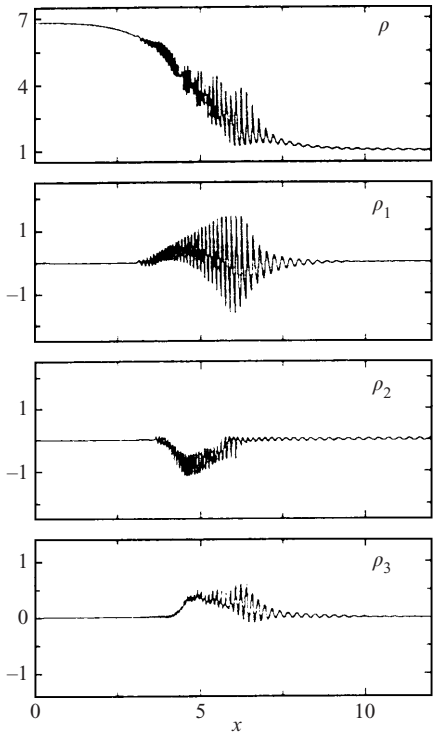

Figure 6. Profiles of ρ, and the wave density perturbations ρ_1, ρ_2 and ρ_3, for the smooth transition shock of Fig. 5 in which an entropy wave (ρ_2) is initially specified upstream of the shock. The diffusion coefficient $\kappa = \kappa_0 = 1$. The profiles are shown at time $t = 10\ \kappa_0/u_0^2$.

where a backward (forward) sound wave is initially specified far upstream of the shock. The plots in Fig. 5 show the wave density profiles for ρ_1, ρ_2 and ρ_3 at time $t = 10\tau_d$, where τ_d is the convection diffusion time scale. The results are similar to those in Fig. 3, except that the backward sound wave is now driven unstable owing to the cosmic ray squeezing instability, whereas the forward sound wave is damped. The difference in the behaviour of the sound waves in Figs 3 and 5 is in accord with the wave mixing coefficient formulae (3.4), which show that the cosmic ray squeezing instability terms depend on $(\rho a_g)^{-1}(\zeta+1)\partial p_c/\partial x$, where $\zeta = \partial \ln \kappa/\partial \ln \rho$ (see also Drury and Falle (1986), for a discussion of the dependence of the squeezing instability on ζ for the case of WKB sound waves). In Fig. 3, $\zeta = -1.5$, whereas $\zeta = 0$ in Fig. 5. In Fig. 6, an entropy wave is initially specified far upstream of the shock. The figure shows the generation of the backward and forward sound waves at time $t = 10\tau_d$, from the initial entropy wave due to wave mixing. The results are similar to those in Fig. 4, except that the backward sound wave now becomes the dominant wave at late times.

Figures 7 and 8 show examples of wave interactions in a cosmic-ray-modified shock with an embedded subshock for the case (6.2) where $\kappa = \kappa_0 = 1$, corresponding to a diffusion coefficient appropriate for a quasiperpendicular shock. The initial conditions correspond to the cases of (a) a backward sound wave incident upon the shock from far upstream (left panels), and (b) a forward sound wave incident upon the shock (right panels). The upstream flow parameters are $M_{l0} = 5.48$ and

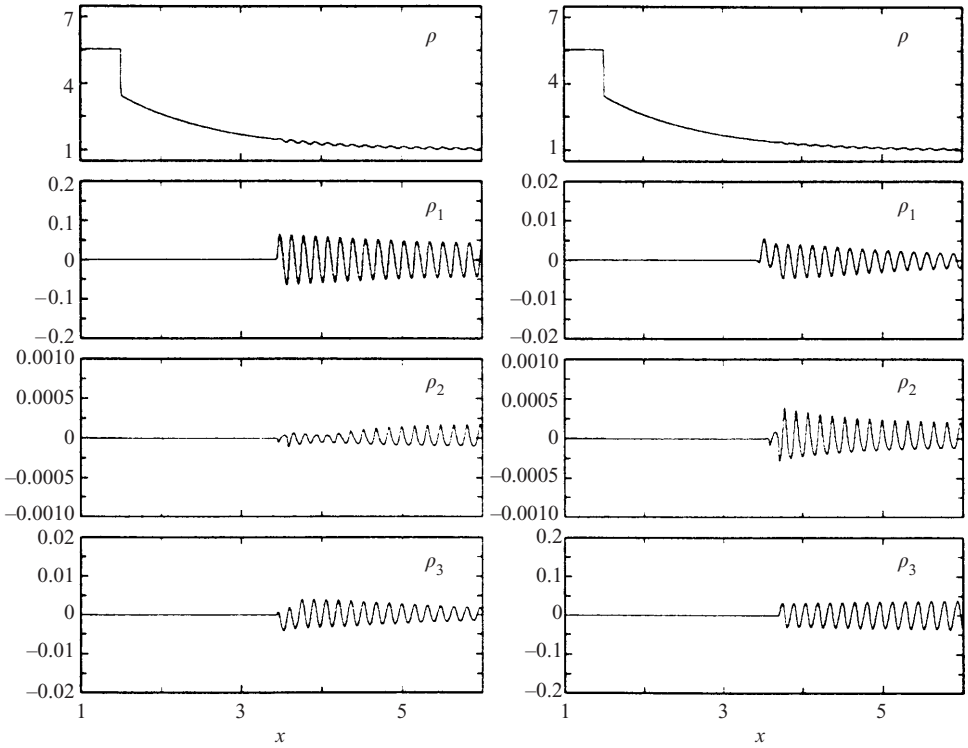

Figure 7. The density perturbations for the backward and forward sound waves (ρ_1 and ρ_3) and the entropy wave (ρ_2) in a cosmic-ray-modified shock, with an embedded subshock. The upstream long-wavelength Mach number $M_{\ell 0} = 5.48$, $p_{c0} = p_{g0} = 1$ far upstream ($x \to \infty$) and $\kappa = 1$. The wave amplitudes are shown at time $t = 0.1$. The left panels correspond to the case where a backward sound wave is initially incident upon the shock from far upstream, whereas in the right panels, a forward sound wave is initially specified far upstream.

$p_{c0}/p_{g0} = 1$ ($x \to \infty$), $\gamma_c = \frac{4}{3}$ and $\gamma_g = \frac{5}{3}$. The density perturbations ρ_1, ρ_2 and ρ_3 of the sound waves and the entropy wave, and the density profile $\rho(x, t)$, are shown at times $t = 0.1 \equiv 0.111\tau_d$ (Fig. 7), and at time $t = 0.6 \equiv 0.666\tau_d$ (Fig. 8), where $\tau_d = \kappa_0/u_0^2$ is the diffusive time scale.

At the earlier time (Fig. 7), the wave profiles of the initial wave (ρ_1 in the left panels and ρ_3 in the right panels) behave as one would expect from the squeezing instability predictions of WKB theory. The generated forward sound wave profile ρ_3 on the left grows as one approaches the shock – as one would perhaps expect, since it is slaved to the larger-amplitude backward wave, which grows with decreasing x. Note that the generated waves (ρ_3 on the left and ρ_1 on the right) are about an order of magnitude smaller than the initial wave. The entropy wave fluctuations are negligible compared with the amplitudes ρ_1 and ρ_3 for the sound waves. The waves in Fig. 7 behave as one would expect from linear wave mixing theory.

Now consider the wave profiles at the later time ($t = 0.6$) in Fig. 8. For the case on the left, the backward wave shows moderate growth due to the squeezing instability. The wave has steepened owing to self wave interaction (Burgers wave steepening) into a sequence of shocklets, with an N-wave profile (for a discussion of nonlinear versions of the wave mixing equations (3.1), see Webb et al. 1997a). The corresponding generated forward sound wave (ρ_3) has a cusped profile, in which

https://doi.org/10.1017/S0022377898007466 Published online by Cambridge University Press

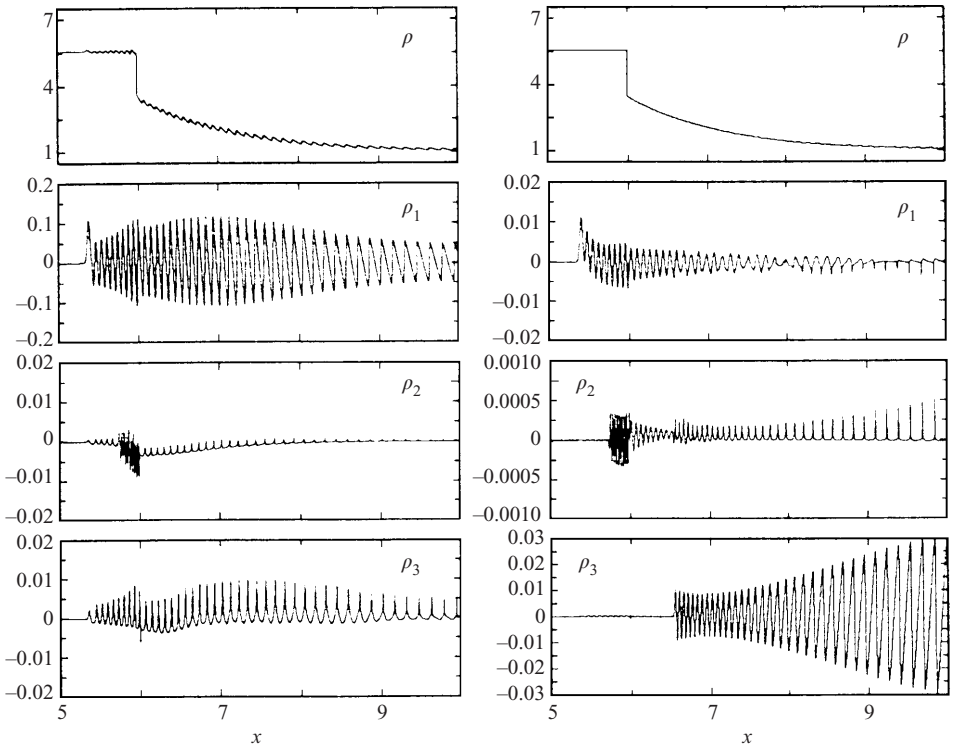

Figure 8. The evolution of the waves in Fig. 7 at a later time $t = 0.6$. Note the development of N-wave profiles for the primary incident waves due to nonlinear wave steepening (incident backward sound wave in the left panels, and incident forward sound wave in the right panels), and the cusped profiles of the generated waves.

the cusps appear at the shocklet locations for the backward wave (ρ_1). There is a jump in the wave amplitudes at the subshock ($x \approx 6$), and entropy waves are generated downstream of the subshock. The structure of the subshock, which is not obvious in the figure, is determined by numerical viscosity in the Zeus 2D code. The generation, transmission and reflection of sound waves, entropy waves and vorticity waves at gas-dynamical shocks has been studied by McKenzie and Westphal (1968) and McKenzie and Bornatici (1974). These effects are clearly evident in the figure, where there are jumps in the wave amplitudes across the subshock.

For the case of an incident forward sound wave (right panels), the forward sound wave is damped by the squeezing instability and generates the backward wave (ρ_1) by wave mixing. Wave steepening results in the formation of shocklets in the forward wave profile (ρ_3), with corresponding jumps in the entropy wave profile (ρ_2) at the shocklets. Note that there is a sharp jump in the ρ_3 amplitude at $x \approx 6.5$. This corresponds to the trailing edge of the initial forward sound wave with phase speed $\lambda_3 = u + a_g$, which has not yet been overtaken by the subshock. The large jump in ρ_3 at $x \approx 6$ at the subshock is a numerical artefact.

It is important to note that more refined kinetic theory models of cosmic-ray-modified shocks (see e.g. Jones and Ellison 1991; Malkov 1997) predict that there are no totally smoothed solutions. However, if the subshock is very weak, the profile of the shock transition may appear to be smooth.

https://doi.org/10.1017/S0022377898007466 Published online by Cambridge University Press

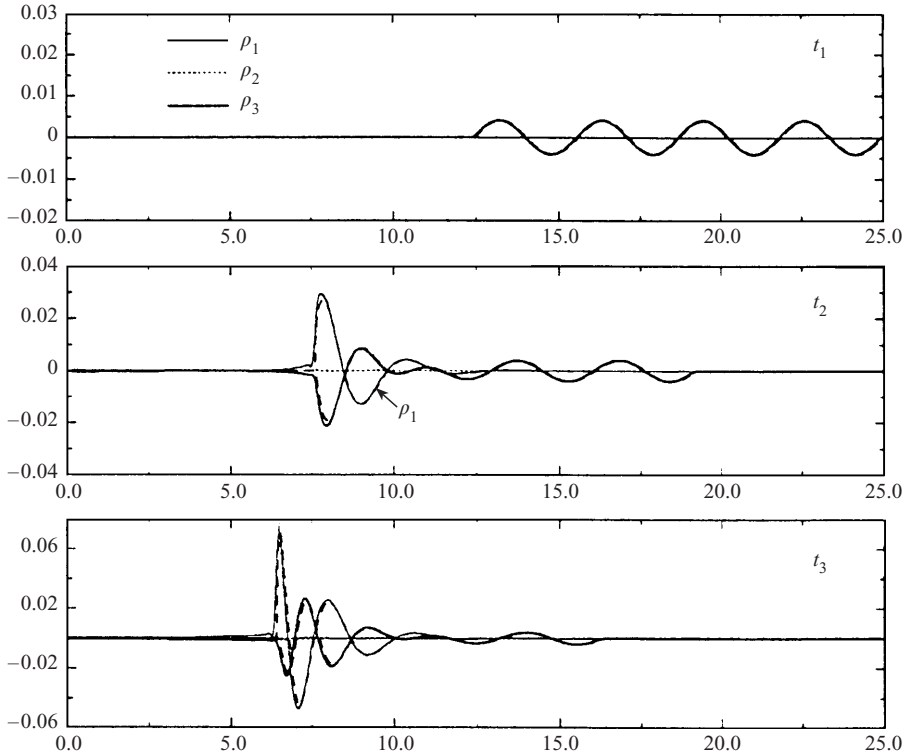

Figure 9. A comparison between spectral code solutions of the wave mixing equations (3.1) (dashed curves) and numerical solutions of the two-fluid equations (2.1)–(2.4) (solid curves and dotted curve), for the smooth transition cosmic ray shock of Fig. 5, with $M_{l0} = 18.26$, $p_{c0}/p_{g0} = 1$, $\gamma_g = \frac{5}{3}$, $\gamma_c = \frac{4}{3}$, and $\kappa = 1$. A forward sound wave is initially specified far upstream at time $t = t_1 = 0$. The two lower panels show the solutions at times $t = t_2 = 0.06$ and $t = t_3 = 0.09$.

6.1.2. Linear wave mixing solutions and WKB solutions. In this subsection, we compare the results obtained using numerical solutions of the linear wave mixing equations (3.1), WKB solutions (Secs 5.3 and 5.4) and the nonlinear simulations (Figs 3–8). Figure 9 shows a comparison of spectral code solutions of the linear wave mixing equations (3.1) (dashed curves) and numerical solutions of the fully nonlinear two-fluid equations (2.1)–(2.4), for the smooth transition shock of Fig. 5, in which $\kappa = 1$, $M_{l0} = 18.26$, $p_{c0}/p_{g0} = 1$, $\gamma_g = \frac{5}{3}$ and $\gamma_c = \frac{4}{3}$. Figure 9 shows the density perturbations ρ_1, ρ_2 and ρ_3 at two time instants $t = t_2 = 0.06$ and $t = t_3 = 0.09$ that result when a forward sound wave train (ρ_3) is initially specified far upstream at time $t = t_1 = 0$. The numerical solutions of the two-fluid equations (2.1)–(2.4) for ρ_1 and ρ_3 are shown by the solid curves. Note that the entropy wave density perturbation $\rho_2 \equiv 0$ in both the fully nonlinear solutions and the spectral code solutions. In the present example, linear wave mixing theory predicts that $\rho_2 = 0$, since the entropy S of the background flow is constant (i.e. $S_x = 0$). In this case, the wave mixing coefficients Λ_{21} and Λ_{23} linking the entropy wave to the sound waves are both zero, and no entropy wave perturbations can be generated from the initial sound wave train. The figure shows that there is excellent agreement between the spectral code solutions of the wave mixing equations (3.1) and the fully nonlinear

https://doi.org/10.1017/S0022377898007466 Published online by Cambridge University Press

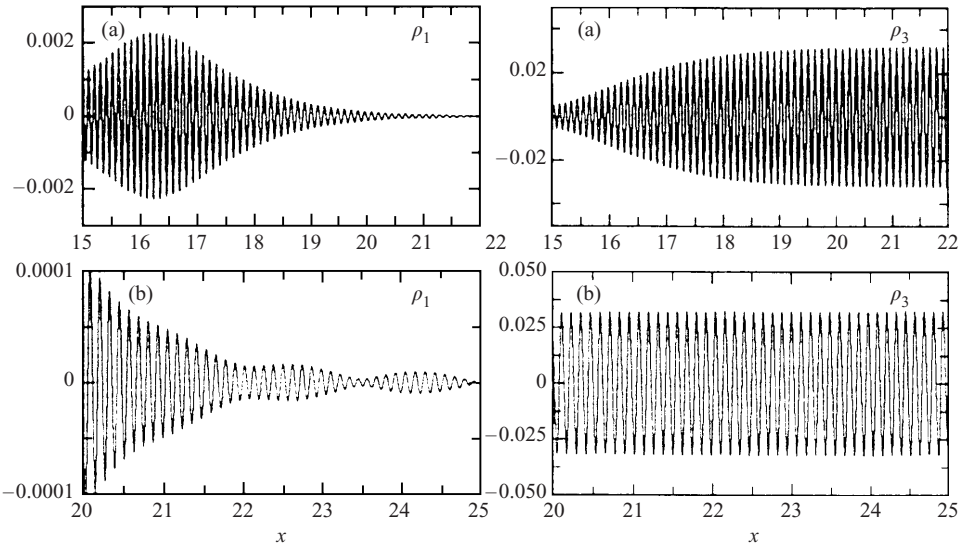

Figure 10. Uniform WKB solutions (5.33), for waves with a constant frequency ω, corresponding to the case where $\rho_3(x,0) = \rho_{30}$, and $\rho_1 = \rho_2 = 0$ at $x = x_0 = 25$, for the same background flow as in Fig. 5. The diffusion coefficient $\kappa = 1$. In the top panels (a), $15 < x < 22$. The bottom panels (b) show an expanded view of the solutions in the region $20 < x < 25$.

numerical solutions of the two-fluid equations (2.1)–(2.4). The agreement between the two sets of solutions is expected, since the amplitude of the initial sound wave is sufficiently small for linear theory to apply. One expects linear theory to break down at large times, when the sound waves steepen and become nonlinear. The results in Fig. 9 are similar to the numerical simulation results in the right panels of Fig. 5, where the initial forward sound wave is damped, and generates the unstable backward sound wave by wave coupling. At late times ($t = t_3$), the generated backward sound wave is dominant.

Figure 10 shows uniform WKB solutions (5.33) for waves with a constant frequency ω, corresponding to the case where $\rho_3 = \rho_{30}$, $\rho_1 = \rho_2 = 0$ at $x = x_0 = 25$, the diffusion coefficient $\kappa = 1$, and for the same background flow as that in Figs 5 and 6. The top panels (a) show the wave profiles for $15 < x < 22$, whereas the lower panels (b) show an expanded view of the waveforms in the far-upstream region $20 < x < 25$. The WKB solutions show excellent agreement with the corresponding solutions obtained by iterating the wave mixing integral equations (5.34) and (5.35) for $x \geqslant 17$. The results are similar to those in Figs 5 and 9, in which a forward sound wave is specified far upstream ($F_0 = 0$ and $G_0 \neq 0$ in (5.31) and (5.32)). The backward wave ρ_1 in the lower panels (b) shows the phenomenon of wave beating. An inspection of (5.31) and (5.33) shows that, far upstream, the WKB solution for ρ_1 consists of two complex exponential terms $\exp[i\omega(\phi_1 \pm \phi_3 - t)]$ of roughly equal amplitudes, where ϕ_1 and ϕ_3 are the phases of the backward and forward waves in (5.12). The wave beating phenomenon is clearly a result of wave mixing between the backward and forward sound waves.

6.2. Wave mixing in cosmic ray pressure balance structures

A cosmic ray pressure balance-solution of the two-fluid equations (2.1)–(2.4) is an equilibrium structure in which the acceleration vector of the fluid is zero (i.e. the

https://doi.org/10.1017/S0022377898007466 Published online by Cambridge University Press

fluid velocity $\mathbf{u}$ is a constant vector), and the sum of the cosmic ray and thermal gas pressures is constant throughout the structure. The solution corresponds to a travelling wave solution in which p_g, ρ, S and p_c are all functions of

$$\bar{x} = x - ut, \tag{6.3}$$

and the fluid speed u is a constant. The entropy advection equation (2.6) allows solutions for $S = S(\bar{x})$ with S a non-trivial function of $\bar{x}$. The cosmic ray pressure $p_c(\bar{x})$ is obtained from solving the cosmic ray energy equation (2.4), which reduces to a steady-state diffusion equation:

$$\frac{d}{d\bar{x}}\left(\kappa\frac{dp_c}{d\bar{x}}\right) = 0, \tag{6.4}$$

where the cosmic ray diffusion coefficient κ is assumed to be a function of $\bar{x}$. For the case

$$\kappa = \kappa_0 \cosh^2\left(\frac{\bar{x}}{L}\right), \tag{6.5}$$

we obtain a solution of (6.4) of the form

$$p_c = p_{c\infty}^- + \tfrac{1}{2}(p_{c\infty}^+ - p_{c\infty}^-)\left[1 + \tanh\left(\frac{\bar{x}}{L}\right)\right], \tag{6.6}$$

where $p_c \to p_{c\infty}^-$ as $\bar{x} \to -\infty$ and $p_c \to p_{c\infty}^+$ as $\bar{x} \to +\infty$. The gas pressure p_g is given by

$$p_g = P_0 - p_c(\bar{x}), \tag{6.7}$$

where $P_0 = p_c + p_g$ is the constant total pressure. Other forms of pressure balance structures (PBS) may be obtained by using other functional forms for the diffusion coefficient $\kappa(\bar{x})$ in (6.5).

6.2.1. Wave mixing. In this subsection, we consider the propagation of short-wavelength sound waves and entropy waves through the steady pressure balance structure described by (6.3)–(6.7). In a convenient abuse of notation, we use x to denote the position variable in the frame of the pressure balance structure (i.e. we use x to replace $\bar{x}$ in the present section). The short-wavelength wave interaction equations (3.1) have a simpler form for steady pressure balance structures, because

$$\Lambda_{12} = \Lambda_{22} = \Lambda_{32} = 0, \tag{6.8}$$

(because u = const in a PBS). In the frame of the PBS, $u = 0$, and the wave interaction equations (3.1) reduce to

$$\frac{\partial \rho_2}{\partial t} + \Lambda_{21}(\rho_1 - \rho_3) = 0, \tag{6.9}$$

$$\frac{\partial \rho_1}{\partial t} - a_g\frac{\partial \rho_1}{\partial x} + \left(\Lambda_{11} - \frac{\partial a_g}{\partial x}\right)\rho_1 + \Lambda_{13}\rho_3 = 0, \tag{6.10}$$

$$\frac{\partial \rho_3}{\partial t} + a_g\frac{\partial \rho_3}{\partial x} + \Lambda_{31}\rho_1 + \left(\Lambda_{33} + \frac{\partial a_g}{\partial x}\right)\rho_3 = 0 \tag{6.11}$$

for the entropy wave, backward sound wave and forward sound wave respectively.

6.2.2. WKB analysis. Suppose the waves have a single frequency ω, so that

$$\rho_j = \Re\{\bar{\rho}_j \exp(-i\omega t)\}, \quad j = 1, 2, 3. \tag{6.12}$$

https://doi.org/10.1017/S0022377898007466 Published online by Cambridge University Press

Following the development of the wave mixing equations for the cosmic-ray-modified shock case of Section 5.1, the wave interaction equations (6.9)–(6.11) reduce to two coupled ordinary differential equations:

$$\frac{d\bar{f}}{dx} = \left(\nu_{11} - i\frac{\omega}{a_g}\right)\bar{f} + \nu_{13}\bar{g}, \tag{6.13}$$

$$\frac{d\bar{g}}{dx} = \nu_{31}\bar{f} + \left(\nu_{33} + i\frac{\omega}{a_g}\right)\bar{g}, \tag{6.14}$$

where

$$\bar{f} = \bar{\rho}_1 I, \qquad \bar{g} = \bar{\rho}_3 I, \tag{6.15a}$$

$$I = (a_g)^{(3\gamma_g-5)/2(\gamma_g-1)}\exp\left(\frac{S}{2(\gamma_g-1)C_v}\right). \tag{6.15b}$$

The interaction coefficients $\{\nu_{ij} : i,j = 1,3\}$ in (6.13) and (6.14) are given by the equations

$$\nu_{11} = \frac{1}{2a_g}\left(\frac{a_c^2}{\kappa} + \frac{a_g}{\gamma_g p_g}\frac{\partial p_c}{\partial x}\right), \tag{6.16a}$$

$$\nu_{33} = -\frac{1}{2a_g}\left(\frac{a_c^2}{\kappa} - \frac{a_g}{\gamma_g p_g}\frac{\partial p_c}{\partial x}\right), \tag{6.16b}$$

$$\nu_{13} = \Phi_x + \nu_{33}, \tag{6.16c}$$

$$\nu_{31} = \Phi_x + \nu_{11}, \tag{6.16d}$$

$$\Phi = \frac{(\gamma_g-2)S}{2\gamma_g(\gamma_g-1)C_v} - \frac{\gamma_g-3}{2(\gamma_g-1)}\ln(a_g). \tag{6.16e}$$

Equations (6.13)–(6.16) describe the sound waves. The solution for the entropy wave,

$$\bar{\rho}_2 = \frac{i}{\omega}\Lambda_{21}(\bar{\rho}_3 - \bar{\rho}_1), \qquad \Lambda_{21} = \frac{a_g S_x}{\gamma_g C_v}, \tag{6.17}$$

may be constructed once the sound wave solutions have been determined.

Equations (6.13) and (6.14) have the same form as (5.8) and (5.9) for cosmic-ray-modified shocks, except that $\nu_{12} = \nu_{32} = 0$ for the PBS solution. Furthermore, the interaction coefficients $\{\nu_{ij} : i,j = 1,3\}$ in (6.16) are analogous to (5.5), but with the mapping $u \mapsto 0$ and $\psi \mapsto \Phi$ relating the coefficients ν_{ij} in (5.5) to those in (6.16). Hence (6.13) and (6.14) for $\bar{f}$ and $\bar{g}$ may be reduced to the equations

$$\frac{d\bar{F}}{dx} = A\bar{G}, \tag{6.18a}$$

$$\frac{d\bar{G}}{dx} = B\bar{F}, \tag{6.18b}$$

where

$$\bar{F} = \exp(-i\omega\phi_1 - \gamma_1)\bar{f}, \tag{6.19a}$$

$$\bar{G} = \exp(-i\omega\phi_3 - \gamma_3)\bar{g}. \tag{6.19b}$$

The interaction coefficients A and B have the form

$$A = \nu_{13}\exp(i\omega\phi + \gamma), \qquad B = \nu_{31}\exp(-i\omega\phi - \gamma), \tag{6.20a}$$

$$\phi = \phi_3 - \phi_1, \qquad \gamma = \gamma_3 - \gamma_1, \tag{6.20b}$$

https://doi.org/10.1017/S0022377898007466 Published online by Cambridge University Press

$$\phi_j = \int_{x_0}^{x} \frac{dx'}{\lambda_j}, \qquad \gamma_j = \int_{x_0}^{x} dx'\, \nu_{jj}, \qquad j = 1, 3, \tag{6.20c}$$

where $\lambda_1 = -a_g$ and $\lambda_3 = a_g$.

From (6.15) and (6.19), we have

$$\bar{\rho}_1 = \frac{\exp(i\omega\phi_1 + \gamma_1)}{I}\bar{F}, \tag{6.21a}$$

$$\bar{\rho}_3 = \frac{\exp(i\omega\phi_3 + \gamma_3)}{I}\bar{G}. \tag{6.21b}$$

Using an integral equation formulation of (6.18) (see Sec. 5.3), it is straightforward to obtain WKB expansions for $\bar{F}$ and $\bar{G}$ for high-frequency waves, and the required WKB solutions for the ρ_j then follow from (6.12) and (6.21). The net results of this analysis are solutions for the ρ_j of the form

$$\rho_1 = \Re\{\hat{\rho}_1(x,t)\}, \tag{6.22a}$$

$$\rho_3 = \Re\{\hat{\rho}_3(x,t)\}, \tag{6.22b}$$

$$\rho_2 = \frac{\Lambda_{21}}{\omega}\Re\{i(\hat{\rho}_3 - \hat{\rho}_1)\}, \tag{6.22c}$$

where

$$\begin{aligned}\hat{\rho}_1(x,t) = \frac{1}{I}\Bigg[&\bar{F}_0 \exp[-i\omega(t-\phi_1)+\gamma_1]\left(1 + \frac{i}{\omega}\int_{x_0}^{x} dy \frac{\nu_{13}(y)\nu_{31}(y)}{\phi_y}\right)\\ &-\frac{i}{\omega}\bar{G}_0\left(\frac{\nu_{13}(x)}{\phi_x}\exp[-i\omega(t-\phi_3)+\gamma_3]\right.\\ &\left.-\frac{\nu_{13}(x_0)}{\phi_{x_0}}\exp[-i\omega(t-\phi_1)+\gamma_1]\right)\Bigg],\end{aligned} \tag{6.23}$$

$$\begin{aligned}\hat{\rho}_3(x,t) = \frac{1}{I}\Bigg[&\bar{G}_0 \exp[-i\omega(t-\phi_3)+\gamma_3]\left(1 - \frac{i}{\omega}\int_{x_0}^{x} dy \frac{\nu_{13}(y)\nu_{31}(y)}{\phi_y}\right)\\ &+\frac{i}{\omega}\bar{F}_0\left(\frac{\nu_{31}(x)}{\phi_x}\exp[-i\omega(t-\phi_1)+\gamma_1]\right.\\ &\left.-\frac{\nu_{31}(x_0)}{\phi_x(x_0)}\exp[-i\omega(t-\phi_3)+\gamma_3]\right)\Bigg],\end{aligned} \tag{6.24}$$

where $\bar{F}_0 \equiv \bar{F}(x_0)$ and $\bar{G}_0 \equiv \bar{G}(x_0)$ are the integration constants in the solutions for $\bar{F}$ and $\bar{G}$.

The main difference between the WKB wave mixing solutions (6.21)–(6.24) and the corresponding results (5.43) and (5.44) for sound waves in cosmic-ray-modified shocks is that the entropy S is a function of x in the pressure balance solutions (6.21)–(6.24), but S = const in the modified shock case. Note also that $u = 0$ in the PBS wave mixing solutions, whereas $u(x)$ is a function of x in the modified shock case. In the PBS wave mixing solutions, the non-zero entropy gradient ($S_x \neq 0$) allows the linear entropy wave to be generated from the sound waves (i.e. $\Lambda_{21} \neq 0$ in (6.22)). The integrating factor I, (6.15), and the sound wave interaction coefficients $\{\nu_{ij} : i, j = 1, 3\}$ for the PBS solutions also depend on $S(x)$.

6.2.3. Numerical examples of waves in pressure balance structures. An example of the interaction of a sound wave with a cosmic ray pressure balance structure in which there is a large-scale entropy gradient is illustrated in Figs 11 and 12. The left panels

https://doi.org/10.1017/S0022377898007466 Published online by Cambridge University Press

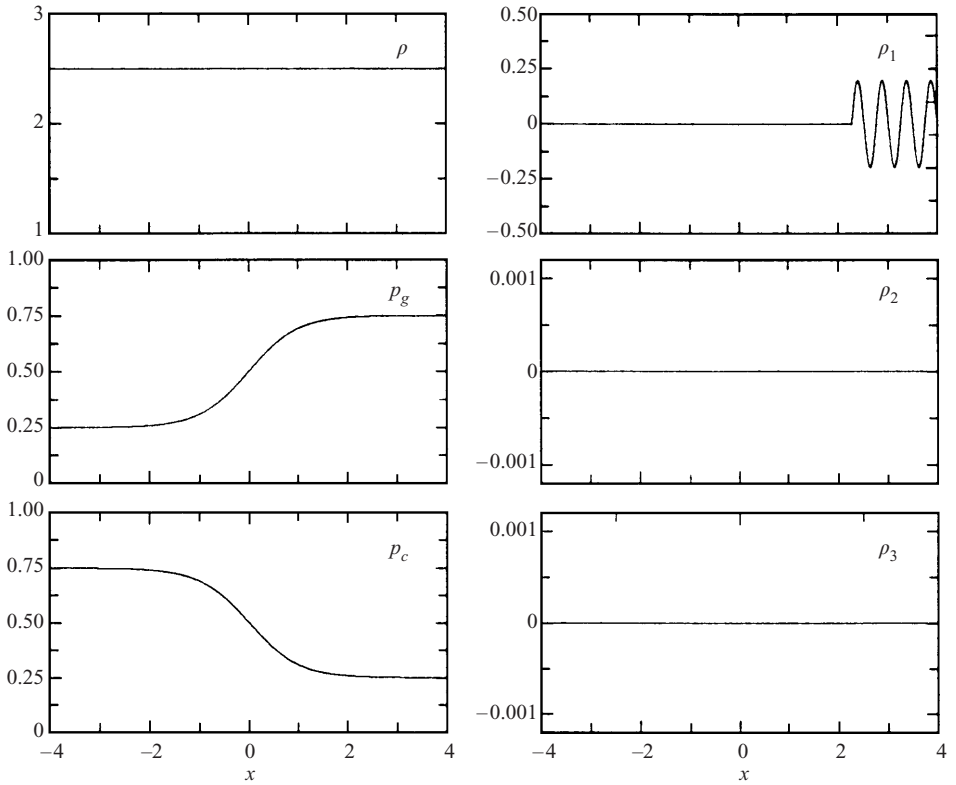

Figure 11. Schematic profiles of ρ, p_g and p_c in a steady cosmic ray pressure balance structure (left panels). The right panels show initial conditions in which a backward sound wave is incident upon the structure from the right. These initial conditions and background state are used in the wave mixing solution examples in Fig. 12.

in Fig. 11 show the density profile (ρ = const), gas pressure profile $p_g(x)$ and cosmic ray pressure profile $p_c(x)$ in a steady state pressure balance structure described by (6.3)–(6.7). The right panels in Fig. 11 show that at time $t = 0$, a backward sound wave is incident on the structure from the right (ρ_1). At time $t = 0$, the entropy wave (ρ_2) and the forward sound wave (ρ_3) perturbations are identically zero.

Figure 12 illustrates how the backward sound wave (ρ_1) initially incident upon the structure generates both the entropy wave (ρ_2) and forward sound wave (ρ_3) by the combined effect of instabilities and wave mixing, at two time instants $t = 4.5$ (left panels) and at time $t = 7.5$ (right panels). The results in Fig. 12 were obtained by solving the wave mixing equations (6.9)–(6.11) as an initial value problem using a spectral code, in which the a backward sound wave is initially incident on the PBS from the right (see Fig. 11). Note that in this linear wave interaction description, the waves do not modify the background flow. The backward sound wave (ρ_1) in Fig. 12 shows wave growth as the wave progresses through the structure, which is due in part to the cosmic ray squeezing instability, but also depends on wave mixing with the other waves. The generated entropy wave (ρ_2) has a significantly larger amplitude than the generated forward sound wave at the later time ($t = 7.5$). The generated forward sound wave and the entropy wave ρ_2 are approximately π out of phase in Fig. 12.

https://doi.org/10.1017/S0022377898007466 Published online by Cambridge University Press

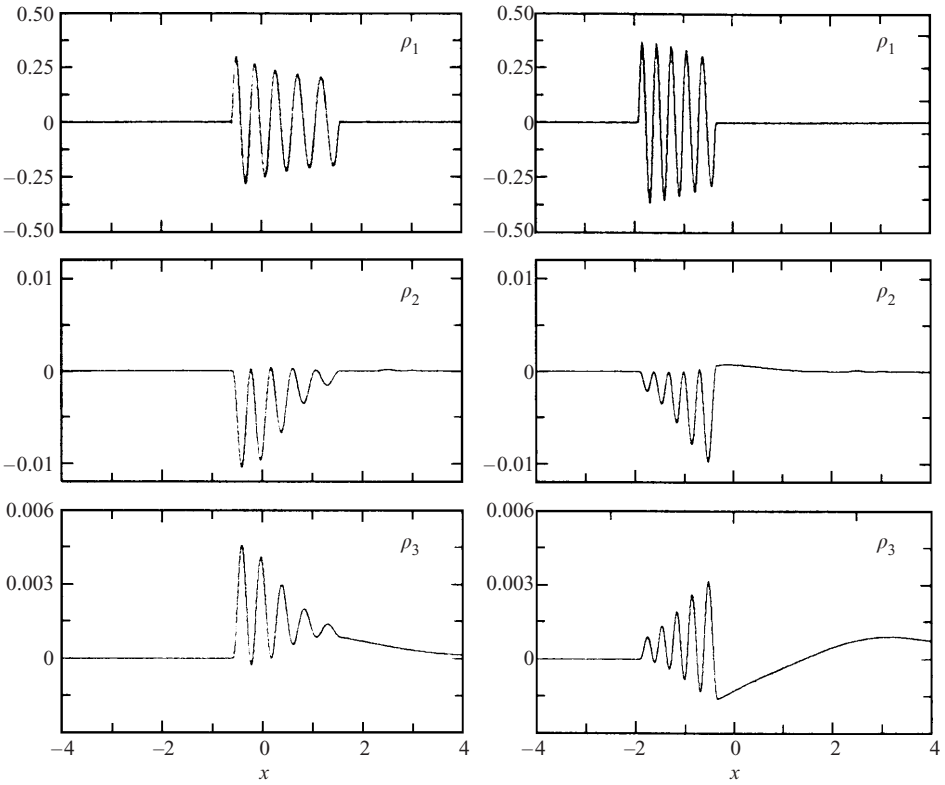

Figure 12. Spectral code solutions of the wave mixing equations (6.9)–(6.11) for the cosmic ray pressure balance structure in Fig. 11, in which a backward sound wave is initially incident on the structure from the right. The diffusion coefficient is given by (6.5). The figure shows the profiles of ρ_1, ρ_2 and ρ_3 at times $t = 4.5$ (left panels) and $t = 7.5$ (right panels). The entropy wave (ρ_2) and the forward sound wave (ρ_3) are generated by wave mixing.

7. Diffusion coefficient estimates and applications

Now consider the possible application of the results in Figs 3–7 to wave instabilities in cosmic-ray-modified supernova remnant (SNR) shocks. A useful discussion of constraints on particle acceleration in supernova remnant shocks is given by Axford (1981). In particular, Axford argues that in order to preserve the spectral form of the secondary nuclei, the bulk of energetic particle acceleration must occur in the hot interstellar medium, and that the primaries are accelerated in relatively strong SNR shocks that occupy less than a few percent of the galactic confining volume. Since the particle acceleration time and confinement time in the galaxy depend on the cosmic ray diffusion tensor $\mathbf{K}$, this implies numerical constraints on $\mathbf{K}$.

In Sec. 7.1, we discuss diffusion coefficient estimates, which we use in Sec. 7.2 to estimate growth rates, and wave mixing rates in cosmic-ray-modified SNR shocks.

7.1. Diffusion coefficient estimates

The magnetohydrodynamic turbulence and waves surrounding supernova remnant shocks, which determine the energetic particle diffusion coefficient $K(\mathbf{r},p)$ (where $\mathbf{r}$ is position and p is the energetic particle momentum), are not well known. Some

https://doi.org/10.1017/S0022377898007466 Published online by Cambridge University Press

authors (e.g. Berezhko and Völk 1997) use a modified form of the Bohm diffusion coefficient:

$$K = \kappa_B \frac{\rho_s}{\rho}, \qquad \kappa_B = \tfrac{1}{3} v r_g, \tag{7.1}$$

where κ_B is the Bohm diffusion coefficient, v is the particle speed, $r_g = pc/ZeB$ is the energetic particle gyro-radius, and ρ_s denotes the value of the density ρ at the shock. For a $T = 1$ GeV proton in a galactic magnetic field of $B = 10^{-6}$ G, (7.1) yields

$$\kappa_B(T = 1 \text{ GeV}) = 4.95 \times 10^{22} \text{ cm}^2 \text{ s}^{-1}, \qquad r_g = 5.65 \times 10^{12} \text{ cm} \tag{7.2}$$

as typical values for the Bohm diffusion coefficient and gyro-radius r_g.

The value of the diffusion coefficient parallel to the background magnetic field $\mathbf{B} = B_0 \mathbf{e}_z$ in quasilinear theory (see e.g. Jokipii 1971; Fisk et al. 1974) depends sensitively on the correlation length L_c of the turbulence, the particle momentum p, the amplitude of the turbulence (i.e. $\delta B/B$, where $(\delta B)^2$ is the mean square magnetic field fluctuation) and the wavenumber (k) dependence of the turbulent power spectrum. The localized turbulence upstream of a supernova remnant shock, which should be due in part to cosmic-ray-generated waves in front of the shock (see e.g. Lerche 1967; Skilling 1975; McKenzie and Völk 1982), will have significantly different characteristics than the diffuse, large-scale turbulence present in the interstellar medium (see e.g. Spangler et al. 1987; Armstrong et al. 1995; Achterberg and Ball 1994). Below, we estimate the diffusion coefficient K_{IS}, associated with the diffuse interstellar turbulence, and the more relevant diffusion coefficient K_{SNR} upstream of a supernova remnant shock.

Using the results of Jokipii (1971), a crude estimate of the diffusion coefficient $K_\parallel$ parallel to the background magnetic field $\mathbf{B} = B_0 \mathbf{e}_z$ due to resonant wave–particle interactions (cyclotron resonance) is

$$K_\parallel = \frac{v\lambda_\parallel}{3} = \kappa_B N \left(\frac{\delta B}{B}\right)^{-2} \frac{r_g}{L_c} \left[H(r_g - L_c) + \left(\frac{r_g}{L_c}\right)^{-n} H(L_c - r_g) \right]. \tag{7.3}$$

In (7.1), v is the particle speed, r_g is the particle gyro-radius, $\lambda_\parallel$ is the particle mean free path parallel to $\mathbf{B}$, $\kappa_B = \frac{1}{3} v r_g$ is the Bohm diffusion coefficient, $H(x)$ is the Heaviside step function and N is a normalization constant given below. In (7.1), the power spectrum $P_{xx}(k)$ of the turbulence has the form $P_{xx}(k) = A(k/k_c)^{-n}$ for $k > k_c$, and $P_{xx}(k) = A$ (A = const) for $k < k_c$, where $k_c = 1/L_c$ is the wavenumber corresponding to the correlation length L_c. Equation (7.3) is based on equations (46) and (57) of Jokipii (1971), and the normalization constant N and δB in (7.3) are given by the equations

$$N = \frac{10n}{\pi(n-1)}, \qquad \delta B^2 = \frac{2}{\pi} \int_0^\infty P_{xx}(k)\, dk \tag{7.4}$$

(note that the equation for δB^2 in (7.4) is a consequence of the definition of $P_{xx}(k)$ used by Jokipii 1971).

As parameters characterizing diffuse interstellar turbulence, we take

$$L_c = 10^{19} \text{ cm}, \qquad \frac{\delta B}{B} = 0.3, \qquad n = \tfrac{5}{3}, \tag{7.5}$$

which yields

$$K = K_{IS} = 6.4 \times 10^{28} \text{ cm}^2 \text{s}^{-1}, \qquad \lambda_\parallel = 7.31 \times 10^{18} \text{ cm} \equiv 2.37 \text{ pc} \tag{7.6}$$

https://doi.org/10.1017/S0022377898007466 Published online by Cambridge University Press

as typical values for K and $\lambda_\parallel$ for $T = 1$ GeV protons in a $B = 10^{-6}$ G magnetic field (note that $n = \frac{5}{3}$ corresponds to Kolmogorov turbulence). For $r_g < L_c$, $K \propto vp^{1/3}$, but $K \propto vp^2$ for $r_g > L_c$. It is of interest to note that a diffusion coefficient of $K \approx 10^{28}$ cm^2 s^{-1} is also required to explain the abundance of secondary nuclei (e.g. Be and B) in galactic cosmic rays (Berezinskii et al. 1990).

Taking $L_c = 5.65 \times 10^{12}$ cm, and $\delta B/B = 0.3$ for the localized turbulence in the vicinity of a supernova remnant shock, (7.3) yields

$$K_\parallel = K_{SNR} = 4.4 \times 10^{24} \text{ cm}^2 \text{ s}^{-1}, \qquad \lambda_\parallel = 5.03 \times 10^{14} \text{ cm} \tag{7.7}$$

for the diffusion coefficient K_{SNR} and mean free path $\lambda_\parallel$ for $T = 1$ GeV protons in a $B = 10^{-6}$ G magnetic field upstream of the shock. This value of K is intermediate between the Bohm diffusion value for K in (7.2) and the value of $K = 10^{26}$ cm^2 s^{-1} at $T = 1$ GeV and $K \propto p^{0.25}$ used by Kang and Jones (1991) in their numerical study of of diffusive particle acceleration at supernova remnant shocks. The diffusion coefficient K_{SNR} in (7.7) is about four orders of magnitude smaller than the diffusion coefficient K_{IS} in (7.6) associated with large-scale transport of cosmic rays in the galaxy. It is important to note that it is difficult to constrain the values of $K_\parallel$ and $\lambda_\parallel$ upstream of supernova remnant shocks without detailed observations of individual supernova remnants. For example, Spangler et al. (1987) found from low-frequency observations of the radio source 1503 + 467 that an upper limit on the thickness of the foreshock region ΔR of the supernova remnant HB9 is less than 3.5% of the shock radius $R = 22$ pc (i.e. $\Delta R < 0.77$ pc).

7.2. Wave mixing and instability growth rates

In order to assess the role of wave mixing and instabilities in supernova remnant shocks, we first rewrite the wave mixing equations in the form

$$\frac{\partial \rho_i}{\partial t} + \lambda_i \frac{\partial \rho_i}{\partial x} = \sum_{j=1}^{3} \mathbf{\Omega}_{ij} \rho_j, \quad i = 1, 2, 3, \tag{7.8}$$

where

$$\mathbf{\Omega}_{ii} = -\mathbf{\Lambda}_{ii} - \frac{\partial \lambda_i}{\partial x}, \qquad \mathbf{\Omega}_{ij} = -\mathbf{\Lambda}_{ij} \quad (i \neq j) \tag{7.9}$$

and the $\{\mathbf{\Lambda}_{ij}\}$ are given in (3.4). The coefficients $\{\mathbf{\Omega}_{ij}\}$ have the dimensions of [time]$^{-1}$. The coefficients $\mathbf{\Omega}_{11}$ and $\mathbf{\Omega}_{33}$ are associated with WKB growth rates of the backward and forward sound waves due to the squeezing instability. For the case of a steady background flow, the wave mixing equations (3.1) may be combined to yield the wave-action-like equation

$$\begin{aligned} &\frac{\partial}{\partial t}(\omega_1 \mathscr{A}_1 + \omega_3 \mathscr{A}_3) + \frac{\partial}{\partial x}(\lambda_1 \omega_1 \mathscr{A}_1 + \lambda_3 \omega_3 \mathscr{A}_3) \\ &= -\frac{\rho_2}{\rho}\frac{du}{dt}(\lambda_1 \rho_1 + \lambda_3 \rho_3) + \tau_{A1}^{-1}\left(\omega_1 \mathscr{A}_1 - \frac{a_g}{\rho}\lambda_3 \rho_1 \rho_3\right) \\ &\quad + \tau_{A3}^{-1}\left(\omega_3 \mathscr{A}_3 + \frac{a_g}{\rho}\lambda_1 \rho_1 \rho_3\right), \end{aligned} \tag{7.10}$$

where

$$\tau_{A1}^{-1} = -\left(\frac{a_c^2}{\kappa} + \frac{\zeta + 1}{\rho a_g}\frac{\partial p_c}{\partial x}\right), \tag{7.11a}$$

https://doi.org/10.1017/S0022377898007466 Published online by Cambridge University Press

$$\tau_{A3}^{-1} = -\left(\frac{a_c^2}{\kappa} - \frac{\zeta+1}{\rho a_g}\frac{\partial p_c}{\partial x}\right), \tag{7.11b}$$

are the growth rates for the wave action densities

$$\mathscr{A}_1 = -\frac{\rho v_1^2}{k_1 a_g}, \tag{7.12a}$$

$$\mathscr{A}_3 = \frac{\rho v_3^2}{k_3 a_g}, \tag{7.12b}$$

for the backward ($\mathscr{A}_1$) and forward ($\mathscr{A}_3$) sound waves, $du/dt = u_t + uu_x$ is the acceleration vector for the background flow, and $\zeta = \partial \ln \kappa / \partial \ln \rho$. In (7.10)–(7.12), $\omega_1 = k_1\lambda_1$ and $\omega_3 = k_3\lambda_3$ are the dispersion equations for the backward and forward sound waves. Equation (7.10) generalizes the WKB wave action equations

$$\frac{\partial \mathscr{A}_j}{\partial t} + \frac{\partial}{\partial x}(\lambda_j \mathscr{A}_j) = \frac{\mathscr{A}_j}{\tau_{Aj}}, \quad j = 1, 3, \tag{7.13}$$

obtained by Drury and Falle (1986) and Zank and McKenzie (1987) describing sound wave instabilities in cosmic-ray-modified flows.

Alternative expressions for τ_{A1}^{-1} and τ_{A3}^{-1} for steady shocks are

$$\tau_{A1}^{-1} = -\frac{a_c^2}{\kappa} - a_g(\zeta+1)(M^2-1)\frac{d\ln\rho}{dx}, \tag{7.14a}$$

$$\tau_{A3}^{-1} = -\frac{a_c^2}{\kappa} + a_g(\zeta+1)(M^2-1)\frac{d\ln\rho}{dx}, \tag{7.14b}$$

where $M = |u/a_g|$ is the sonic Mach number of the flow in the shock frame. The results (7.14) are a consequence of the steady-state shock structure equations (see e.g. Axford et al. 1982). The results (7.14) emphasize the role of the sonic Mach number on the instability growth rates.

The wave mixing coefficients $\{\Omega_{1j}\}$ and $\{\Omega_{3j}\}$, $j = 1, 2, 3$, and wave action growth rates τ_{A1}^{-1} and τ_{A3}^{-1} for the smooth transition cosmic-ray-modified shock of Fig. 3 are displayed in Fig. 13. The diffusion coefficient has the form (6.1) (i.e. $\kappa \propto \rho^{-3/2}$), which is probably a reasonable form for the dependence of κ for a quasiparallel shock. The corresponding results for the the same shock, but with $\kappa = \kappa_0 = \text{const}$, thought to be appropriate for a quasiperpendicular shock, are shown in Fig. 14. The figures show how the dimensionlesss wave mixing coefficients $\bar{\Omega}_{1j} = \tau_d \Omega_{1j}$ and $\bar{\Omega}_{3j} = \tau_d \Omega_{3j}$ and wave action growth rates $\bar{\tau}_{Aj}^{-1} = \tau_d \tau_{Aj}^{-1}$ vary throughout the shock structure, where $\tau_d = \kappa_0/u_0^2$ is the diffusive time scale and u_0 is the shock speed. The wave action growth rates have approximately twice the amplitudes of the wave interaction coefficients $\{\Omega_{ij}\}$, which are of order τ_d^{-1} in the present examples.

The coefficients $\{\Omega_{1j} : j = 1, 2, 3\}$ and the wave action growth rate τ_{A1}^{-1} for the backward sound wave in the left panels of Fig. 13 are negative in the upstream shock precursor, where $\partial p_c/\partial x$ is significant. The coefficients are all of the same order of magnitude, and are dominated by the cosmic ray pressure gradient contributions in the centres of the profiles. Far upstream and downstream of the shock, where the gradients are negligible, $\Omega_{11} \approx \Omega_{33} = -a_c^2/2\kappa$, $\Omega_{13} \approx \Omega_{31} = a_c^2/2\kappa$, and $\Omega_{12} = \Omega_{32} \approx 0$, where a_c is the cosmic ray sound speed. Similar results are obtained for the forward sound wave (the right panels of Fig. 13), except that the wave mixing coefficients just upstream of the shock are now positive. This implies that a

https://doi.org/10.1017/S0022377898007466 Published online by Cambridge University Press

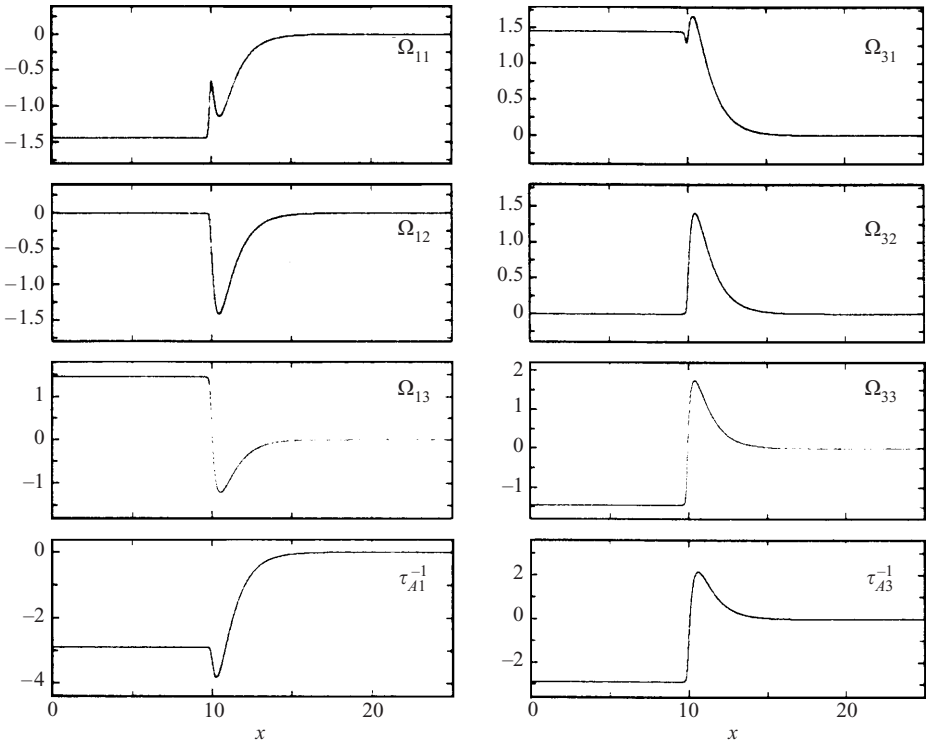

Figure 13. Wave mixing coefficients $\{\Omega_{1j} : j = 1, 2, 3\}$ and wave action growth rate τ_{A1}^{-1} for the backward sound wave (left panels), and the corresponding coefficients $\{\Omega_{3j} : j = 1, 2, 3\}$ and rate τ_{A3}^{-1} for the forward sound wave (right panels) for the smooth transition, cosmic-ray-modified shock in Fig. 3. The diffusion coefficient $\kappa = \kappa_0(\rho/\rho_0)^{-3/2}$, with $\kappa_0 = 1$ in computational units. The rates are given in units of τ_d^{-1}, where $\tau_d = \kappa_0/u_0^2$ is the convection diffusion time scale, and the abscissa x is given in units of the convection diffusion scale $l_d = \kappa_0/u_0$.

forward sound wave upstream of the shock is driven unstable owing to the cosmic ray squeezing instability.

The corresponding results for $\kappa = \kappa_0 = \text{const}$, appropriate for a perpendicular shock, in Fig. 14 show that the backward wave upstream of the shock is driven unstable, whereas a forward sound wave upstream of the shock is damped. This is opposite to the predictions for a quasiparallel shock (Fig. 13), where the forward sound wave is unstable, and the backward sound wave is damped. The difference between the results in Figs 13 and 14 is due solely to the difference in the density dependence of the diffusion coefficient κ in the two cases.

As an application of the above results, consider the propagation of a cosmic-ray-modified SNR shock in the warm interstellar medium with

$$T = 10^4 \text{ K}, \quad n = 0.2 \text{ cm}^{-3}, \quad B = 10^{-6} \text{ G}, \quad \kappa = K_{SNR}\left(\frac{\rho}{\rho_0}\right)^{-3/2} \text{ cm}^2 \text{ s}^{-1}, \tag{7.15}$$

where T and n denote the temperature and number density of the thermal gas far upstream of the shock and $K_{SNR} = 4.4 \times 10^{24}$ cm^2 s^{-1}, as in (7.7). Using the above parameters as typical of the upstream medium and assuming $p_{c0} = p_{g0}$, we

https://doi.org/10.1017/S0022377898007466 Published online by Cambridge University Press

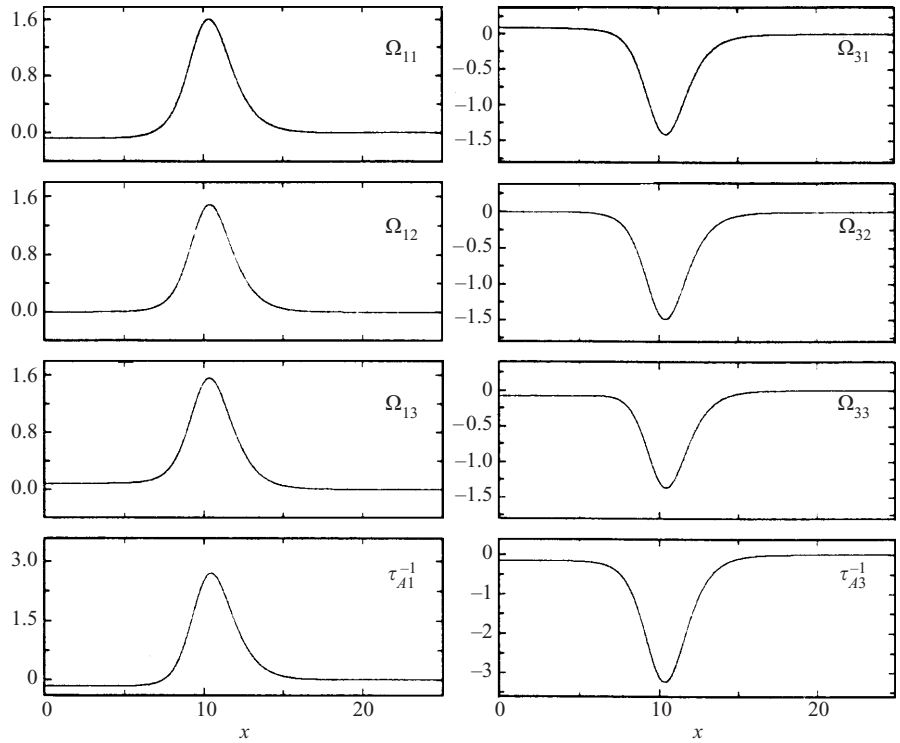

Figure 14. Same as Fig. 13, except for the cosmic-ray-modified shock of Fig. 5, with $\kappa = 1$, in computational units. Far upstream, $M_{l0} = 18.26$ and $p_{c0}/p_{g0} = 1$.

obtain $p_{c0} = p_{g0} = 5.52 \times 10^{-13}$ dyn cm^{-2} upstream of the shock. The cosmic ray sound speed a_{c0}, gas sound speed a_{g0}, and Alfvén speed V_{A0} have the values $a_{c0} = 14.84$ km s^{-1}, $a_{g0} = 15.84$ km s^{-1} and $V_{A0} = 6.3$ km s^{-1}. Although the two-fluid model in this paper does not include the role of the magnetic field, a rough estimate of its effect can be obtained by using the modified long-wavelength sound speed $a_{*0} = (a_{g0}^2 + a_{c0}^2 + V_{A0}^2)^{1/2}$. In the present case, $a_{*0} \approx 22.6$ km s^{-1}.

For the shock in Fig. 3, with long-wavelength Mach number $M_{l0} = 18.26$, we obtain $u_0 = 413$ km s^{-1} as the shock speed. The convection diffusion time scale $\tau_d = \kappa_0/u_0^2$, length scale $l_d = \kappa_0/u_0$ and cosmic ray damping time $\tau_{cr} = \kappa_0/a_{c0}^2$ then have the values

$$\tau_d \approx 8.184 \times 10^1 \text{ years}, \quad l_d \approx 0.0345 \text{ pc}, \quad \tau_{cr} \approx 6.16 \times 10^4 \text{ years}. \tag{7.16}$$

The maximum growth rate in Fig. 13 is $\Omega_{33} \approx 1.6\tau_d^{-1}$. Using the estimate for τ_d in (7.16), this implies $\Omega_{33} < 1.97 \times 10^{-2}$ year^{-1}, or a minimum growth time of $\tau_{33} = 1/\Omega_{33} \approx 50.9$ years. Note that this growth time is approximately 10^3 times smaller than τ_{cr}, indicating vigorous wave growth in the upstream shock precursor.

Now consider a shock with $M_{l0} = 5.48$, the above values for p_{c0} and p_{g0}, and a diffusion coefficient and upstream parameters as in (7.15). In this case, we obtain

$$u_0 \approx 123.8 \text{ km s}^{-1}, \quad \tau_d = 9.06 \times 10^2 \text{ years}, \quad l_d \approx 0.115 \text{ pc}. \tag{7.17}$$

The maximum growth rate in this case is $\Omega_{33} \approx 0.6\tau_d^{-1} = 6.69 \times 10^{-4}$ year^{-1}, which corresponds to to a minimum growth time $\tau_{33} \approx 1.49 \times 10^3$ years. This growth

https://doi.org/10.1017/S0022377898007466 Published online by Cambridge University Press

Table 1. Instability growth rates and characteristics of the cosmic-ray-modified shock in Fig. 3 and for a shock with $M_{l0} = 5.48$, (7.17), in which the diffusion coefficient $\kappa \propto \rho^{-3/2}$ for the warm ISM model (7.15). The maximum growth rate (Ω_{33}) and minimum growth time (τ_{33}) for the forward sound wave are given in the last two columns.

M_{l0}	u_0 (km s^{-1})	τ_d (yr)	l_d (pc)	Ω_{33} (yr^{-1})	τ_{33} (yr)
18.26	413	81.84	3.45×10^{-2}	1.97×10^{-2}	50.9
5.48	124	906.0	0.115	6.69×10^{-4}	1.495×10^{3}

Table 2. Same as Table 1, except for the hot ISM model (7.18).

M_{l0}	u_0 (km s^{-1})	τ_d (yr)	l_d (pc)	Ω_{33} (yr^{-1})	τ_{33} (yr)
18.26	3475	1.155	4.1×10^{-3}	1.386	0.722
5.48	1043	12.82	1.36×10^{-2}	4.69×10^{-2}	21.34

rate is substantially smaller than the the growth rates for the higher-Mach-number shock with $M_{l0} = 18.26$ of Figs 3 and 13. A summary of these results is given in Table 1.

It is of interest to compare the instability characteristics in Table 1 for the warm ISM model (7.15) with the growth rates expected if the shocks were propagating through the hot interstellar medium (HISM). The characteristic parameters that we adopt for the HISM (e.g. Axford 1981) are

$$T = 7 \times 10^5 \text{ K}, \qquad n = 3 \times 10^{-3} \text{ cm}^{-3},$$

$$B = 10^{-6} \text{ G}, \qquad \kappa = K_{SNR} \left(\frac{\rho}{\rho_0} \right)^{-3/2} \text{ cm}^2\text{s}^{-1}, \tag{7.18}$$

where $K_{SNR} = 4.4 \times 10^{24}$ cm^2 s^{-1}. Taking $p_{c0} = p_{g0}$ far upstream of the shock, we obtain $p_{c0} = p_{g0} = 5.8 \times 10^{-13}$ dyn cm^{-2}. This corresponds to the values $a_{g0} = 139$ km s^{-1}, $a_{c0} = 124$ km s^{-1}, $V_{A0} = 39.85$ km s^{-1} and $a_{*0} = 190.3$ km s^{-1} for the characteristic wave speeds upstream of the shock. Because the shock speeds ($u_0 = 3475$ km s^{-1} for $M_{l0} = 18.26$, and $u_0 = 1043$ km s^{-1} for $M_{l0} = 5.48$) are larger than for the warm ISM model (7.15) by a factor of order 10, τ_d and l_d are roughly smaller by factors of 10^{-2} and 10^{-1} respectively compared with the warm ISM model values in Table 1. The characteristics of the instability for the HISM model (7.18) are summarized in Table 2. It is worth noting that for the case of a very cold upstream gas, the instability growth rate Ω_{33} can be many times τ_d^{-1} (see e.g. Webb (1989), where examples with $\Omega_{33} \approx 100\tau_d^{-1}$ were obtained).

8. Discussion and concluding remarks

The main aim of this paper has been a study of short-wavelength instabilities, wave mixing and nonlinear wave interactions in cosmic-ray-modified shocks.

The short-wavelength squeezing instability for sound waves upstream of a cosmic-ray-modified shock was first investigated by Drury and Falle (1986), Dorfi and Drury (1985) and Zank and McKenzie (1987). Webb et al. (1997a,b,c) (see also Sec. 3) discussed the modification of the squeezing instability by wave mixing, nonlinear wave steepening and nonlinear wave interactions.

The wave mixing equations indicate that, even for a uniform background flow, the backward and forward sound waves are coupled and damped by the cosmic

https://doi.org/10.1017/S0022377898007466 Published online by Cambridge University Press

rays. The coupling coefficient in this case is $\alpha = a_c^2/2\bar{\kappa}$, where $a_c = (\gamma_c p_c/\rho)^{1/2}$ is the cosmic ray sound speed and $\bar{\kappa}$ is the hydrodynamical cosmic ray diffusion coefficient. A Green-function solution illustrating the coupling of the sound waves for a uniform background flow has been investigated in Sec. 4. An initial delta function density spike for the backward wave ρ_1 results in the generation of an approximately top-hat density profile ρ_3 for the forward sound wave, and the generation of a backward sound wave density wake, due to wave interactions. The wakes are limited to the region between the backward and forward sound wave characteristics, and at late times assume bell-shaped profiles (Fig. 2).

High-frequency WKB expansions describing wave mixing in non-uniform flows have been developed in Sec. 5. In the high-frequency limit ($\omega \to \infty$), the WKB results for the squeezing instability are obtained. In this limit, the waves are decoupled and the instability results of Drury and Falle (1986), Dorfi and Drury (1985) and Zank and McKenzie (1987) are obtained. Both a differential equations approach and an integral equation approach to WKB expansions of the wave mixing solutions have been developed for the case of a steady background flow. The integral equation approach, in its simplest form, yields more physically transparent formulae for wave generation due to wave mixing, but the solutions are non-uniform, and are only accurate close to the point where the waves are first generated from the primary wave. The differential equations approach yields more accurate, uniform WKB expansions, but results in less physically transparent formulae. Nayfeh (1973, Chap. 7) discusses resummation or renormalized perturbation techniques to obtain uniform perturbation expansions.

For the case of the propagation of sound waves in an inhomogeneous, isentropic, background flow, in which there are no entropy waves present, the lowest-order WKB solution consists of the primary WKB sound wave (the backward sound wave, say) plus a secondary wave generated by wave mixing (the forward sound wave), with amplitude $O(1/\omega)$ that of the primary wave, and with a phase shift of approximately $\pm\frac{1}{2}\pi$ relative to the primary wave near the point of generation: (5.43) and (5.44). Similar WKB results have been obtained for the generation of backward and forward sound waves from entropy waves, (5.45) and (5.46), in a steady, isentropic background flow.

Numerical simulations of wave interactions in cosmic-ray-modified shocks with both smooth and subshock transitions have been investigated in Sec. 6 (Figs 3–10). Two diffusion coefficient cases were considered, namely (a) $\kappa = \kappa_0(\rho/\rho_0)^{-3/2}$ and (b) $\kappa = \kappa_0 = \text{const}$. Case (a) corresponds to a quasiparallel shock configuration in which $\kappa \propto 1/P_w$, where the Alfvén wave pressure P_w of the scattering wave field in the upstream medium varies as $P_w \propto \rho^{3/2}$. Case (b), with $\kappa = \text{const}$, corresponds to a quasiperpendicular shock, in which the diffusion of particles across the field is due to random walk of the field lines (see e.g. Jokipii 1971). The character of the cosmic ray squeezing instability depends on the density dependence of $\kappa(\rho)$, via the parameter $\zeta = \partial \ln \kappa/\partial \ln \rho$. For cases where $\zeta < -1$ (see e.g. Figs 3 and 4, where $\kappa \propto \rho^{-3/2}$), the forward sound wave upstream of a cosmic-ray-modified shock is driven unstable by the squeezing instability, whereas the backward sound wave is damped. A forward sound wave initially incident upstream of the shock in Fig. 3 ($\kappa \propto \rho^{-3/2}$, right panel), is amplified by the squeezing instability, and the backward sound wave is generated by wave mixing. If there is no large-scale entropy gradient, the linear theory predicts that entropy waves cannot be generated from the sound waves by wave mixing. This

result is verified by the numerical simulations. However, if the sound waves become nonlinear, entropy wave disturbances are generated. In the case where a backward sound wave is initially present in the upstream medium and $\kappa \propto \rho^{-3/2}$, the initial sound wave is damped by the squeezing instability, and generates a forward sound wave by wave mixing. The forward sound wave is subsequently driven unstable by the squeezing instability (Fig. 3, left panel). Figures 5–8 illustrate wave interactions for the diffusion coefficient case $\kappa = \kappa_0 = \text{const}$. In this case, $\zeta > -1$ (in fact, $\zeta = 0$), and the backward sound wave is driven unstable by the squeezing instability, and the forward sound wave is damped. Nonlinear wave steepening in the subshock examples (Figs 7 and 8) leads to N-wave type profiles for the initial sound wave, and distorted, cusped wave profiles for the generated waves.

Numerical solutions of the linear wave mixing equations in a steady, smooth transition cosmic ray shock, in which the initial data includes small-amplitude waves (Fig. 9), result in wave profiles that are in excellent agreement with the fully nonlinear simulations. The uniform WKB wave mixing solutions (5.33) for the sound waves also show excellent agreement with the numerical solutions of the wave mixing equations, for the case of high-frequency sound waves initially incident upstream of the shock. In the far-upstream region, wave beating effects between the backward and forward sound waves occur (Fig. 10). The examples of wave mixing in cosmic ray pressure balance structures (Figs 11 and 12) illustrate the role of a large-scale entropy gradient on the wave mixing of the entropy wave.

An assessment of the role of wave mixing and the cosmic ray squeezing instablity in supernova remnant shocks has been carried out (Sec. 7). The wave mixing coefficients and wave action growth rates (Figs 13 and 14) are of order τ_d^{-1} (where $\tau_d = \kappa_0/u_0^2$ is the convection diffusion time associated with the cosmic-ray-modified shock, where κ_0 is the hydrodynamical cosmic ray diffusion coefficient far upstream of the shock and u_0 is the shock speed), for model parameters thought to be appropriate for the warm interstellar medium (WISM) and the hot interstellar medium (HISM). The main results of interest are summarized in Tables 1 and 2. Typical values of the minimum instability growth times for shocks in the HISM are $\tau_{33} \approx 0.72$ years for the high-Mach-number shock example ($u_0 = 3475$ km s^{-1}, $M_{l0} = 18.26$, where M_{l0} is the long-wavelength Mach number of the shock), and $\tau_{33} \approx 21$ years for a lower-Mach-number shock ($u_0 = 1043$ km s^{-1} and $M_{l0} = 5.48$). Larger growth times (of order 10 times the above growth times) were obtained for shocks with the same values for M_{l0} propagating through the warm interstellar medium. These results depend on the value of κ used in the analysis. The diffusion coefficient $\kappa \equiv \kappa_{SNR}$ associated with turbulence in the vicinity of supernova remnant shocks is much smaller than the diffusion coefficient describing the large-scale transport of cosmic rays in the galaxy, which is associated with the diffuse, large-scale turbulence in the interstellar medium (see e.g. Spangler et al. 1987; Armstrong et al. 1995). In the examples, we assumed a value of $\kappa_{SNR} \approx 4.4 \times 10^{24}$ cm^2 s^{-1} upstream of the shock, which is intermediate between the values of $\kappa \approx 10^{22}$–10^{23} cm^2 s^{-1}, for Bohm diffusion for protons with $T = 1$ GeV energy, and $\kappa \approx 10^{28}$ cm^2 s^{-1} at $T = 1$ GeV, based on quasilinear theory for cosmic ray diffusion (Jokipii 1971) and observations of the diffuse interstellar turbulence (Armstrong et al. 1995). From radio observations, Spangler et al. (1987), provide an upper limit for the thickness of the foreshock ΔR, of the

supernova remnant HB9 of 3.5% of the shock radius R ($R = 22$ pc and $\Delta R = 0.77$ pc). The thickness of the foreshock in our examples can be identified with the precursor scale length upstream of the shock, $l_d = \kappa_0/u_0^2$. These measurements help to delimit the range of acceptable diffusion coefficients κ_0 upstream of SNR shocks.

Our analysis of the cosmic ray squeezing instability neglects the role of Landau damping of magnetosonic waves in high-beta ($\beta \geqslant 1$) collisionless plasmas (Barnes 1966, 1979) and the role of wave damping of Alfvén waves by ion–neutral friction (Kulsrud and Pierce 1969). In a more self-consistent description, it is also necessary to take into account the momentum spectrum of the cosmic rays. These effects are difficult to include in the two-fluid model used in the present analysis.

The generation, transmission and reflection of sound waves, entropy waves and vorticity eigenmodes at gas-dynamical shocks has been investigated by McKenzie and Westphal (1968) and McKenzie and Bornatici (1974). Presumably, these results, and studies of the interaction of Alfvén waves with MHD shocks (McKenzie and Westphal 1969; Scholer and Belcher 1971; McKenzie and Bornatici 1974), are related to wave mixing phenomena, and must play a role at cosmic ray shocks with embedded subshocks. These issues, and the interaction of MHD waves with cosmic ray modified shocks (e.g. at the solar wind termination shock or at supernova remnant shocks) are worth further investigation.

Acknowledgements

We acknowledge stimulating discussions with M. Brio, J. R. Jokipii and C. P. Sonett. We also acknowledge useful suggestions by one of the referees. The work of G. M. W. was supported in part by NASA Grant NAG-55164. A. Z. was supported in part by NSF Grant ATM 9520135. G. P. Z. is supported in part at the Bartol Research Institute by NSF–DOE Award ATM-9713223, and in part by an NSF Young Investigator Award ATM 9357861.

Appendix A

In this appendix, we discuss the derivation of the solutions (4.9)–(4.12). Introducing the Laplace transforms

$$\bar{\rho}_j(x,s) = \int_0^\infty \exp(-st)\rho_j(x,t)\,dt, \quad j = 1,3, \tag{A 1}$$

the initial value problem (4.1)–(4.4) for the wave mixing equations (4.1) and (4.2) reduces to solving the equations

$$\frac{d}{dx}\begin{pmatrix}\bar{\rho}_1\\ \bar{\rho}_3\end{pmatrix} + \mathbf{A}\begin{pmatrix}\bar{\rho}_1\\ \bar{\rho}_3\end{pmatrix} = \begin{pmatrix}\rho_1(x,0)/\lambda_1\\ \rho_3(x,0)/\lambda_3\end{pmatrix} = \begin{pmatrix}Q_1\\ Q_3\end{pmatrix}, \tag{A 2}$$

where

$$\mathbf{A} = \begin{pmatrix}\dfrac{\alpha+s}{\lambda_1} & -\dfrac{\alpha}{\lambda_1}\\ -\dfrac{\alpha}{\lambda_3} & \dfrac{\alpha+s}{\lambda_3}\end{pmatrix}. \tag{A 3}$$

The homogeneous system (A 2) has solutions

$$\begin{pmatrix}\bar{\rho}_1\\ \bar{\rho}_3\end{pmatrix} = \mathbf{R}\exp(kx), \tag{A 4}$$

where

$$(\mathbf{A} + k\mathbf{I}) \cdot \mathbf{R} = 0. \tag{A 5}$$

Equation (A 5) has non-trivial solutions for $\mathbf{R}$ if

$$\det(\mathbf{A} + k\mathbf{I}) = k^2 + \frac{(s+\alpha)(\lambda_1 + \lambda_3)}{\lambda_1 \lambda_3} k + \frac{(s+\alpha)^2 - \alpha^2}{\lambda_1 \lambda_3} = 0. \tag{A 6}$$

The eigenvalue equation (A 6) has solutions for k of the form

$$k = k_{1,2} = \frac{-M\sigma \mp [\sigma^2 + (M^2-1)\alpha^2]^{1/2}}{a_g(M^2-1)}, \tag{A 7}$$

where

$$M = \frac{u}{a_g}, \qquad \sigma = s + \alpha. \tag{A 8}$$

To solve the inhomogeneous system (A 2), we also need to determine the left-eigenvector solutions of (A 5) satisfying the equations

$$\mathbf{L} \cdot (\mathbf{A} + k\mathbf{I}) = 0, \qquad \mathbf{L}_q \cdot \mathbf{R}_p = \delta^p{}_q, \tag{A 9}$$

where $\delta^p{}_q$ is the Kronecker delta. Searching for solutions of the inhomogeneous equations (A 2) of the form

$$(\bar{\rho}_1, \bar{\rho}_3)^{\mathrm{T}} = \sum_{p=1}^{2} A_p \mathbf{R}_p \exp(k_p x) \tag{A 10}$$

yields the equations

$$\sum_{p=1}^{2} \exp(k_p x)\, \mathbf{R}_p \frac{dA_p}{dx} = \mathbf{Q}. \tag{A 11}$$

Multiplying (A 11) on the left by the left-eigenvector $\mathbf{L}_m$ yields the compatibility conditions

$$\frac{dA_m}{dx} = \exp(-k_m x)\, \mathbf{L}_m \cdot \mathbf{Q}, \quad m = 1, 2 \tag{A 12}$$

with solutions of the form

$$A_m(x) = c_m + \int^x \mathbf{L}_m \cdot \mathbf{Q} \exp(-k_m x')dx', \quad m = 1, 2, \tag{A 13}$$

where the integration constants are determined by the boundary conditions imposed on the solution (A 10) as $|x| \to \infty$. The required solution for $(\bar{\rho}_1, \bar{\rho}_3)^{\mathrm{T}}$ now follows from (A 10) and (A 13).

The right- and left-eigenvectors of (A 5) and (A 9) for $k = k_1$ are

$$\mathbf{R}_1 = \left(1, \frac{\sigma - \Delta^{1/2}}{\alpha(M+1)}\right)^{\mathrm{T}}, \tag{A 14a}$$

$$\mathbf{L}_1 = \frac{1}{2\Delta^{1/2}}(\sigma + \Delta^{1/2}, -\alpha(M+1)), \tag{A 14b}$$

where

$$k_1 = \frac{-M\sigma - \Delta^{1/2}}{a_g(M^2-1)}, \qquad \Delta = \sigma^2 + (M^2-1)\alpha^2. \tag{A 15}$$

https://doi.org/10.1017/S0022377898007466 Published online by Cambridge University Press

The corresponding results for $k = k_2$ are

$$\mathbf{R}_2 = \left(1, \frac{\sigma + \Delta^{1/2}}{\alpha(M+1)}\right)^{\mathrm{T}}, \tag{A 16a}$$

$$\mathbf{L}_2 = \frac{1}{2\Delta^{1/2}}(\Delta^{1/2} - \sigma, (M+1)\alpha), \qquad k_2 = \frac{\Delta^{1/2} - M\sigma}{a_g(M^2-1)}. \tag{A 16b}$$

where

$$k_2 = \frac{\Delta^{1/2} - M\sigma}{a - g(M^2-1)}. \tag{A 17}$$

A.1. Subsonic flow solution

For subsonic flow ($0 < M < 1$), $k_1 > 0$ and $k_2 < 0$. Since we require $|\bar{\rho}_j| \to 0$ as $|x| \to \infty$ ($j = 1, 3$), (A 10) and (A 13) and the eigenvector results (A 14)–(A 17) yield the solutions

$$\bar{\rho}_1 = \frac{\exp(\sigma M\tilde{x} - \Delta^{1/2}|\tilde{x}|)}{2\Delta^{1/2}a_g}\left(\alpha N_3 + \frac{\sigma - \Delta^{1/2}}{1-M}N_1\right) + \frac{N_1}{(1-M)a_g}\exp(\sigma M\tilde{x} - \Delta^{1/2}|\tilde{x}|)\, H(-x), \tag{A 18}$$

$$\bar{\rho}_3 = \exp(\sigma M\tilde{x} - \Delta^{1/2}|\tilde{x}|)\left(\alpha N_1 + \frac{\sigma - \Delta^{1/2}}{M+1}N_3\right) + \frac{N_3}{(M+1)a_g}\exp(\sigma M\tilde{x} - \Delta^{1/2})\, H(x), \tag{A 19}$$

where

$$\tilde{x} = \frac{x}{a_g|1-M^2|} \tag{A 20}$$

and $H(x)$ is the Heaviside step function.

Using the inverse Laplace transforms

$$\mathscr{L}^{-1}\left\{\frac{\exp[-b(p^2-\alpha^2)^{1/2}]}{(p^2-\alpha^2)^{1/2}}\right\} = I_0[\alpha(t^2-b^2)^{1/2}]H(t-b), \tag{A 21a}$$

$$\mathscr{L}^{-1}\left\{\exp[-b(p^2-\alpha^2)^{1/2}]\left(\frac{p}{(p^2-\alpha^2)^{1/2}} - 1\right)\right\} = \alpha\left(\frac{t-b}{t+b}\right)^{1/2} I_1[\alpha(t^2-b^2)^{1/2}]H(t-b), \tag{A 21b}$$

$$\mathscr{L}^{-1}\{\exp[-b(p^2-\alpha^2)^{1/2}] - \exp(-bp)\} = \frac{\alpha b}{(t^2-b^2)^{1/2}} I_1[\alpha(t^2-b^2)^{1/2}]H(t-b), \tag{A 21c}$$

$$\mathscr{L}^{-1}\{\exp(-pb)\} = \delta(t-b), \tag{A 21d}$$

(Erdelyi et al. 1954, Vol. 1, p. 249, formulae 36, 38 and 35), the Laplace inversion of (A 18) and (A 19) yields the solutions (4.10) and (4.13). In (A 21),

$$\mathscr{L}^{-1}\{F(p)\} = \frac{1}{2\pi i}\int_{c-i\infty}^{c+i\infty} \exp(pt)\, F(p)\, dp \tag{A 22}$$

denotes the inverse Laplace transform of $F(p)$.

https://doi.org/10.1017/S0022377898007466 Published online by Cambridge University Press

A.2. Supersonic flow case

For the supersonic flow case, we find $0 > k_2 > k_1$, and the solution only exists downstream of the source (i.e. for $x > 0$). The solutions for $\bar{\rho}_1$ and $\bar{\rho}_3$ for $x > 0$ are

$$\bar{\rho}_1 = \frac{\exp[-(\sigma M + \Delta^{1/2})\tilde{x}]}{2a_g}\left[\frac{N_1}{M-1}\left(\frac{\sigma}{\Delta^{1/2}}+1\right) - \frac{\alpha N_3}{\Delta^{1/2}}\right] + \frac{\exp[(\Delta^{1/2} - \sigma M)\tilde{x}]}{2a_g}\left[\frac{N_1}{M-1}\left(1-\frac{\sigma}{\Delta^{1/2}}\right) + \frac{\alpha N_3}{\Delta^{1/2}}\right], \tag{A 23}$$

$$\bar{\rho}_3 = \frac{\exp[-(\sigma M + \Delta^{1/2})\tilde{x}]}{2a_g}\left[\frac{N_3}{M+1}\left(1-\frac{\sigma}{\Delta^{1/2}}\right) - \frac{\alpha N_1}{\Delta^{1/2}}\right] + \frac{\exp[(\Delta^{1/2} - \sigma M)\tilde{x}]}{2a_g}\left[\frac{N_3}{M+1}\left(\frac{\sigma}{\Delta^{1/2}}+1\right) + \frac{\alpha N_1}{\Delta^{1/2}}\right]. \tag{A 24}$$

The inverse Laplace transform of (A 23) and (A 24) again leads to the solutions (4.10)–(4.13). The inversion of (A 22) and (A 23) involves some transforms not listed in Erdelyi et al. (1954), which result in modified and ordinary Bessel functions in the time domain. However, the ordinary Bessel function contributions to the solution cancel, leading to the solutions (4.10)–(4.13).

Appendix B

In this appendix, we point out some misprints in Webb et al. (1997a). Equations (5.53b) and (5.53d) of the above paper should read

$$S_0'' + 2S_0'S_1' - (i\phi_x S_1' + M_{13}S_0') = 0, \tag{B 1}$$

$$S_2'' + 2S_1'S_2' + 2S_0'S_3' - (i\phi_x S_3' + M_{13}S_2') = 0. \tag{B 2}$$

As noted in the second paragraph of Sec. 5 of the present paper, some initial value terms were missing in Webb et al. (1997a) in the matching of the backward and forward sound wave solutions, for sound waves in an inhomogeneous flow, in which there are no entropy waves present. The more exact matching conditions for the backward and forward sound waves are given in (5.31)–(5.33) of the present paper.

Appendix C

In this appendix, we discuss alternative integral equation formulations for (5.14)–(5.19). Probably the simplest integral equation formulation is to directly integrate (5.14) and (5.15) to obtain the vector integral equation

$$\boldsymbol{\Psi}(x,\omega) = \int_{x_0}^{x} \mathbf{M}(y,\omega)\cdot\boldsymbol{\Psi}(y,\omega)\,dy + \boldsymbol{\Psi}^0(x,\omega), \tag{C 1}$$

where

$$\boldsymbol{\Psi} = \begin{pmatrix} F \\ G \end{pmatrix}, \quad \mathbf{M} = \begin{pmatrix} 0 & A \\ B & 0 \end{pmatrix}, \tag{C 2}$$

and

$$\boldsymbol{\Psi}^0 = \boldsymbol{\Psi}_0 + \int_{x_0}^{x} \mathbf{Q}(y)dy, \quad \mathbf{Q} = \begin{pmatrix} Q_1 \\ Q_3 \end{pmatrix}. \tag{C 3}$$

Equation (C 1) is a Volterra integral equation for $\boldsymbol{\Psi}$.

https://doi.org/10.1017/S0022377898007466 Published online by Cambridge University Press

Alternatively, starting from (5.17) and (5.18), we may obtain Volterra integral equations for $\Phi = \bar{F}_{xx}$ and $\Gamma = \bar{G}_{xx}$. To proceed, we first note

$$\bar{F}_{xx} = \Phi, \tag{C 4a}$$

$$\bar{F}_x = \int_{x_0}^{x} \Phi(y)\, dy + \bar{F}_0', \tag{C 4b}$$

$$\bar{F} = \int_{x_0}^{x} (x-y)\Phi(y) dy + x\bar{F}_0' + \bar{F}_0, \tag{C 4c}$$

where $\bar{F}_0 = \bar{F}(x_0)$ and $\bar{F}_0' = \bar{F}'(x_0)$ are the values of $\bar{F}$ and $d\bar{F}/dx$ at $x = x_0$. From (5.14),

$$\bar{F}_0' = A(x_0)\bar{G}_0 + Q_1(x_0). \tag{C 5}$$

Equation (5.17) may now be expressed in the form of a Volterra integral equation:

$$\Phi(x) - \int_{x_0}^{x} M(x,y)\Phi(y)\, dy = \Phi^0(x), \tag{C 6}$$

where the kernel $M(x,y)$ and source term $\Phi^0(x)$ are given by the equations

$$M(x,y) = D_x(\ln A) + (x-y)A(x)B(x), \tag{C 7}$$

$$\Phi^0(x) = S_F + \bar{F}_0' D_x(\ln A) + A(x)B(x)(\bar{F}_0 + x\bar{F}_0'). \tag{C 8}$$

Similarly, we find that $\Gamma = \bar{G}_{xx}$ satisfies the Volterra integral equation

$$\Gamma(x) - \int_{x_0}^{x} N(x,y)\Gamma(y)\, dy = \Gamma^0(x), \tag{C 9}$$

where the kernel $N(x,y)$ and the source $\Gamma^0(x)$ are given by

$$N(x,y) = D_x(\ln B) + (x-y)A(x)B(x), \tag{C 10}$$

$$\Gamma^0(x) = S_G + \bar{G}_0' D_x(\ln B) + A(x)B(x)(\bar{G}_0 + x\bar{G}_0'), \tag{C 11}$$

and the equations

$$\Gamma = \bar{G}_{xx}, \tag{C 12a}$$

$$\bar{G}_x = \int_{x_0}^{x} \Gamma(y)\, dy + \bar{G}_0', \tag{C 12b}$$

$$\bar{G} = \int_{x_0}^{x} (x-y)\Gamma(y)\, dy + x\bar{G}_0' + \bar{G}_0, \tag{C 12c}$$

$$\bar{G}_0' = B(x_0)\bar{F}_0 + Q_3(x_0) \equiv \nu_{31}(x_0)\bar{F}_0 + Q_3(x_0) \tag{C 12d}$$

relate $\bar{G}$, $\bar{G}_x$ and $\bar{G}_{xx}$ to Γ and the initial conditions. Equations (C 6) and (C 9) can be solved by iteration to find solutions for $\Phi(x)$ and $\Gamma(x)$. The solutions for $\bar{F}$ and $\bar{G}$ then follow from (C 4) and (C 12).

References

Achterberg, A. and Ball, L. 1994 Particle acceleration at superluminal, quasi-perpendicular shocks. application to SN 1978K and SN 1987A. *Astron. Astrophys.* **285**, 687.

Armstrong, J. W., Rickett, B. J. and Spangler, S. R. 1995 Electron density power spectrum in the local interstellar medium. *Astrophys. J.* **443**, 209.

Axford, W. I. 1981 Acceleration of cosmic rays by shock waves. In: *Proceedings of 17th Interntional Cosmic Ray Conference, Paris*, Vol. 12, p. 155.

https://doi.org/10.1017/S0022377898007466 Published online by Cambridge University Press

Axford, W. I., Leer, E. and Skadron, G. 1977 Acceleration of cosmic rays by shock waves. In: *Proceedings of 15th International Cosmic Ray Conference, Plovdiv, Bulgaria*, Vol. 11 (ed. Ch. Ya Christov, P. N. Markov and B. L. Betev), p. 132. Bulgarian Academy of Sciences.

Axford, W. I., Leer, E. and McKenzie, J. F. 1982 The structure of cosmic ray shocks. *Astron. Astrophys.* **111**, 317.

Barnes, A. 1966 Collisionless damping of hydromagnetic waves. *Phys. Fluids* **9**, 1483.

Barnes, A. 1979 Hydromagnetic waves and turbulence, in the solar wind. In: *Solar System Plasma Physics*, Vol. 1 (E. N. Parker, C. F. Kennel and L. J. Lanzerotti), p. 250. North-Holland, Amsterdam.

Begelman, M. C. and Zweibel, E. G. 1994 Acoustic instability driven by cosmic ray streaming. *Astrophys. J.* **431**, 689.

Bell, A. R. 1978 The acceleration of cosmic rays in shock fronts, I. *Mon. Not. R. Astron. Soc.* **182**, 147.

Berezhko, E. G. 1986 Instability in a shock passing through a gas with a cosmic ray pressure component, *Soviet. Astron. Lett.* **12**, 352.

Berezinskii, V. S., Bulanov, S. V., Dogiel, V. A., Ginzburg, V. L. and Ptuskin, V. S. (eds) 1990 *Astrophysics of Cosmic Rays*. North-Holland, Amsterdam.

Blandford, R. D. and Ostriker, J. P. 1978 Particle acceleration by astrophysical shocks. *Astrophys. J. Lett.* **221**, L29.

Chalov, S. V. 1988 Diffusive shock instability in plasma modified by cosmic rays. *Soviet Astron. Lett.* **14**, 114.

Dolginov, A. Z. and Toptygin, I. N. 1967 Diffusion of cosmic particles in the interplanetary medium. *Geomagn Aeron.* **7**, 785.

Donohue, D. J. and Zank, G. P. 1993 Steady state and dynamical structure of a cosmic ray modified termination shock. *J. Geophys. Res.* **98**, 19005.

Dorfi, E. A. and Drury, L. O'C. 1985 A cosmic ray driven instability. In: *Proceedings of 19th International Cosmic Ray Conference, La Jolla, CA*, Vol. 3 (ed. F. C. Jones, J. Adams and G. M. Mason), p. 121. NASA Conf. Publ. 2376.

Drury, L. O'C. and Falle, S. A. E. G. 1986 On the stability of shocks modified by particle acceleration. *Mon. Not. R. Astron. Soc.* **223**, 353.

Drury, L. O'C. and Völk, H. J. 1981 Hydromagnetic shock structure in the presence of cosmic rays. *Astrophys. J.* **248**, 344.

Ellison, D. C. 1981 Monte Carlo simulations of charged particles upstream of the Earth's bow shock. *Geophys. Res. Lett.* **9**, 991.

Ellison, D. C. 1985 Shock acceleration of diffuse ions at the Earth's bow shock: acceleration efficiency and A/Z enhancement. *J. Geophys. Res.* **90**, 29.

Erdelyi, A., Magnus, W., Oberhettinger, F. and Tricomi, G. 1954 *Tables of Integral Transforms*, Vol. 1. McGraw-Hill, New York.

Fisk, L. A., Goldstein, M. L., Klimas, A. J. and Sandri, G. 1974 The Fokker Planck coefficient for pitch angle scattering of cosmic rays. *Astrophys. J.* **190**, 417.

Gleeson, L. J. and Axford, W. I. 1967 Cosmic rays in the interplanetary medium. *Astrophys. J. Lett.* **149**, L115.

Heinemann, M. and Olbert, S. 1980 Non-WKB Alfvén waves in the solar wind. *J. Geophys. Res.* **85**, 1311.

Hollweg, J. V. 1996 Non-WKB Alfvén waves in the solar wind: propagation and reflection of pulses. In: *Solar Wind 8* (ed. D. Winterhalter, J. T. Gosling, S. R. Habbal, W. S. Kurth and M. Neugebauer). *AIP Conf. Proc.* **382**, 327.

Jokipii, J. R. 1966 Cosmic ray propagation I. Charged particles in a random magnetic field. *Astrophys. J.* **146**, 480.

Jokipii, J. R. 1971 Propagation of cosmic rays in the solar wind. *Rev. Geophys. Space Phys.* **9**, 27.

Jones, F. C. and Ellison, D. C. 1991 The plasma physics of shock acceleration. *Space Sci. Rev.*, **58**, 259.

Kang, H. and Jones, T. W. 1991 Numerical studies of particle acceleration in supernova remnants. *Mon. Not. R. Astron. Soc.*, **249**, 439-51.

Kang, H., Jones, T. W. and Ryu, D. 1992 Acoustic instability in cosmic ray mediated shocks, *Astrophys. J.*, **385**, 193.

Ko, C. M. and Jeng, A. T. 1994 Magnetohydrodynamic instability driven by cosmic rays. *J. Plasma Phys.* **52**, 23.

Krymsky, G. F. 1964 *Geomagn. Aeron.* **4**, 977.

Krymsky, G. F. 1977 *Dokl. Akad. Nauk. SSSR* **234**, 1306.

Lerche, I. 1967, Unstable magnetosonic waves in a relativistic plasma. *Astrophys. J.* **147**, 689.

McKenzie, J. F. and Westphal, K. O. 1968 Interaction of linear waves with oblique shock waves. *Phys. Fluids* **11**, 2350.

McKenzie, J. F. and Westphal, K. O. 1969 Transmission of Alfvén waves through the Earth's bow shock. *Planet. Space Sci.* **17**, 1029.

McKenzie, J. F. and Bornatici, M. 1974 Effect of sound waves, Alfvén waves, and heat flow on interplanetary shock waves. *J. Geophys. Res.*, **79**, 4589.

McKenzie, J. F. and Völk, H. J. 1982 Nonlinear theory of cosmic ray shocks including self generated Alfvén waves. *Astron. Astrophys.* **116**, 191.

McKenzie, J. F. and Webb, G. M. 1984 Magnetohydrodynamic instability driven by Alfvén waves excited by cosmic rays. *J. Plasma Phys.* **31**, 275.

Malkov, M. A. 1997 Analytic solution for nonlinear shock acceleration in the Bohm limit. *Astrophys. J.*, **485**, 638.

Nayfeh, A. 1973 *Perturbation Methods*. Wiley, New York.

Parker, E. N. 1965 The passage of energetic charged particles through interplanetary space. *Planet. Space. Sci*, **13**, 9.

Scholer, M. and Belcher, J. W. 1971 The effect of Alfvén waves on MHD fast shocks. *Solar Phys.* **16**, 472.

Skilling, J. A. 1975 Cosmic ray streaming – I. Effect of Alfvén waves on particles. *Mon. Not. R. Astron. Soc.* **172**, 557.

Spangler, S. R., Fey, A. and Cordes, J. M. 1987 VLA and low frequency VLBI observations of the radio source 053+467: austere constraints on interstellar scattering in two media. *Astrophys. J.* **322**, 909.

Völk, H. J., Drury. L. O'C. and McKenzie, J. F. 1984 Hydromagnetic estimates of cosmic ray acceleration efficiencies in shock waves, *Astron. Astrophys.* **130**, 19.

Webb, G. M. 1989 On wave stability in relativistic cosmic ray hydrodynamics. *Astrophys. J.* **341**, 767.

Webb, G. M., Brio, M., Zank, G. P. and Story, T. R. 1995 Contact and pressure balance structures in two-fluid cosmic ray hydrodynamics. *Astrophys. J.* **442**, 822.

Webb, G. M., Brio, M., Zank, G. P. and Story, T. R. 1997a Wave–wave interactions in two-fluid cosmic-ray hydrodynamics. *J. Plasma Phys.* **57**, 631.

Webb, G. M., Brio, M. and Zank, G. P. 1997b Short wavelength wave interactions in two fluid cosmic ray hydrodynamics and gas dynamics. In: *Proceedings of 25th International Cosmic Ray Conference, Durban, RSA*, Vol. 6 (ed. M. S. Potgieter, B. C. Raubenheimer and D. J. Van der Walt), p. 429.

Webb, G. M., Zakharian, A. and Zank, G. P. 1997c Short wavelength instabilities in cosmic ray modified shocks. In: *Proceedings of 25th International Cosmic Ray Conference, Durban, RSA*, Vol. 6 (ed. M. S. Potgieter, B. C. Raubenheimer and D. J. Van der Walt), p. 369.

Webb, G. M., Brio, M. and Zank, G. P. 1998 Lagrangian and Hamiltonian aspects of wave mixing in non-uniform media: waves on strings and waves in gas dynamics. *J. Plasma Phys.* **60**, 341.

Webb, G. M., Zakharian, A., Brio, M. and Zank, G. P. 1999 Wave interactions in magneto-hydrodynamics and cosmic-ray-modified shocks. *J. Plasma Phys.* **61**, 295.

Zank, G. P. 1989 A cosmic ray driven plasma instability. *J. Plasma Phys.* **41**, 89.

Zank, G. P. and McKenzie, J. F. 1987 Short wavelength compressive instabilities in cosmic ray shocks and heat conduction flows. *J. Plasma Phys.* **37**, 347.

Zank, G. P., Axford, W. I. and McKenzie, J. F. 1990 Instabilities in energetic particle modified shocks. *Astron. Astrophys.* **233**, 275.

Zhou, Y. and Matthaeus, W. H. 1990 Transport and turbulence modelling of solar wind fluctuations, *J. Geophys. Res.* **95**, 10291.